# Fifth-Order A-WENO Path-Conservative Central-Upwind Scheme for Behavioral Non-Equilibrium Traffic Models

Shaoshuai Chu[1], Alexander Kurganov[1,2,*], Saeed Mohammadian[3] and Zuduo Zheng[3]

[1] *Department of Mathematics, Southern University of Science and Technology, Shenzhen, 518055, P.R. China.*
[2] *Shenzhen International Center for Mathematics and Guangdong Provincial Key Laboratory of Computational Science and Material Design, Southern University of Science and Technology, Shenzhen, 518055, P.R. China.*
[3] *School of Civil Engineering, the University of Queensland, Brisbane Qld, 4072, Australia.*

**Abstract.** Non-equilibrium hyperbolic traffic models can be derived as continuum approximations of car-following models and in many cases the resulting continuum models are non-conservative. This leads to numerical difficulties, which seem to have discouraged further development of complex behavioral continuum models, which is a significant research need.

In this paper, we develop a robust numerical scheme that solves hyperbolic traffic flow models based on their non-conservative form. We develop a fifth-order alternative weighted essentially non-oscillatory (A-WENO) finite-difference scheme based on the path-conservative central-upwind (PCCU) method for several non-equilibrium traffic flow models. In order to treat the non-conservative product terms, we use a path-conservative technique. To this end, we first apply the recently proposed second-order finite-volume PCCU scheme to the traffic flow models, and then extend this scheme to the fifth-order of accuracy via the finite-difference A-WENO framework. The designed schemes are applied to three different traffic flow models and tested on a number of challenging numerical examples. Both schemes produce quite accurate results though the resolution achieved by the fifth-order A-WENO scheme is higher. The proposed scheme in this paper sets the stage for developing more robust and complex continuum traffic flow models with respect to human psychological factors.

*Corresponding author.* *Email addresses:* chuss2019@mail.sustech.edu.cn (S. Chu), alexander@sustech.edu.cn (A. Kurganov), s.mohammadian@uq.edu.au (S. Mohammadian), zuduo.zheng@uq.edu.au (Z. Zheng)

## 1   Introduction

This paper is focused on the development of robust and highly accurate numerical methods for non-equilibrium continuum traffic flow models, as non-conservative systems of hyperbolic PDEs.

Continuum models treat traffic flow as a compressible fluid, and study its behavior using aggregated state variables (for instance, flow and density) and are useful for real-world traffic regarding operation and control [48]. Numerous continuum models have been developed over time to accommodate various empirical and behavioral aspects of traffic flow (see [47] for a critical review), which can be categorized into two broad families of equilibrium and non-equilibrium models.

Equilibrium models rely primarily on the differential forms of the mass conservation principle and some explicit functional forms between the state-variables (that is, speed and density). The most prominent example is the seminal Lighthill-Whitham-Richards (LWR) model [40, 54], which for a section of homogeneous road without intersections, can be presented as

$$\rho_t + (\rho V)_x = 0, \quad V = V_e(\rho), \tag{1.1}$$

where $x$ is the spatial variable, $t$ is the time, $\rho(x,t)$ is the density, and $V_e(\rho)$ describes traffic speed as a generic function of local traffic density. The standard LWR model treats the multi-lane traffic as a single-pipe, assuming all vehicles and drivers have the same properties. Over time, numerous extensions of the LWR model have been proposed to incorporate various aspects such as multi-lane driving and lane-changing manoeuvres (see, e.g., [15,16,25,29]), different vehicle types (see, e.g., [4,49,53,61,62,64]), and drivers' non-local anticipation of traffic condition ahead (see, e.g., [5,10,11,57]).

Regardless of their underlying rationales, all equilibrium models are derived from the flow conservation principles, and thus, can always be presented in the form of the system of balance laws:

$$\boldsymbol{U}_t + \boldsymbol{F}(\boldsymbol{U})_x = \boldsymbol{S}(\boldsymbol{U}), \tag{1.2}$$

where $\boldsymbol{U}$ are the state variables, $\boldsymbol{F}$ are the nonlinear fluxes, and $\boldsymbol{S}(\boldsymbol{U})$ are the source terms. Therefore, equilibrium models are often solved using numerical methods for hyperbolic conservation and balance laws; see, e.g., [20,35,44,69].

Non-equilibrium models, on the other hand, use the same flow continuity equation as in (1.1), but with the speed adapted as a dynamic process. The majority of non-equilibrium models can be presented in the following generic form:

$$\begin{cases} \rho_t + (\rho V)_x = 0, \\ V_t + V V_x = f(\rho, V, \rho_x, V_x, \cdots). \end{cases}$$

These models are particularly useful for capturing some complex traffic phenomena such as emergence of traffic instabilities [60], capacity drop phenomenon downstream the ramp areas [51], and the hysteresis effects [67]. Some non-equilibrium models are phenomenological and are derived directly from fluid mechanics concepts (see, e.g., [13,37]), whereas others are derived from the gas-kinetic theory (see, e.g., [26,59]), or car-following relations (see, e.g., [27,65,70,71]). The majority of existing non-equilibrium models can be formulated in the conservative form (1.2), in which case, the aforementioned numerical methods can be implemented.

However, the conservative form cannot necessarily be guaranteed for certain non-equilibrium models. Lack of the conservation property is likely to be the case when non-equilibrium models are derived from car-following models (see, e.g., [23,24,65,71] and the review paper [55]) and behavioral premises, rather then from conservation principles [68]. In such case, the central idea is to incorporate human psychological factors (for instance, driver memory) into the car-following models as time-dependent ODEs and then to derive a continuum approximation in the Eulerian coordinates. Such practice often results in the emergence of non-conservative products.

The non-conservative traffic flow models can be presented in the following form:

$$\boldsymbol{U}_t + \boldsymbol{F}(\boldsymbol{U})_x = B(\boldsymbol{U})\boldsymbol{U}_x + \boldsymbol{S}(\boldsymbol{U}), \tag{1.3}$$

or in the equivalent quasi-linear form:

$$\boldsymbol{U}_t + \mathcal{A}(\boldsymbol{U})\boldsymbol{U}_x = \boldsymbol{S}(\boldsymbol{U}), \tag{1.4}$$

where $\mathcal{A}(\boldsymbol{U}) = A(\boldsymbol{U}) - B(\boldsymbol{U})$ and $A(\boldsymbol{U}) := \frac{\partial \boldsymbol{F}(\boldsymbol{U})}{\partial \boldsymbol{U}}$ is the Jacobian. Development of such behavioral non-equilibrium non-conservative models is an important research direction as numerous empirical observations have established behavioral foundations for many complex traffic phenomena such as traffic oscillations and hysteresis phenomena (see, e.g., [8,56]). However, the inherent numerical difficulties associated with non-conservative hyperbolic systems has remained an obstacle from an implementation perspective, thereby hindering the development of such urgently needed behavioral continuum models.

To the best of our knowledge, traffic flow models of the form (1.3) or (1.4) have only been investigated analytically: this is possible since even though the models described by the system (1.4) are non-conservative, they are analytically tractable since the matrix $\mathcal{A}$ is known. However, no rigorous numerical studies of these models have been conducted.

In general, development of accurate and robust numerical methods for (1.3) is a challenging task due to the presence of non-conservative product terms. When $\boldsymbol{U}$ is discontinuous, weak solution of the system (1.3) cannot be understood in the sense of distributions. Instead, one can introduce weak solutions in the sense of Borel measures as it was done in [17,38,39], and later used to introduce a concept of path-conservative finite-volume methods; see, e.g., the review papers [6,52] and reference therein.

This paper aims to develop a robust numerical scheme for non-conservative traffic flow behavioral models, and thereby to pave the way for further development of behavioral non-equilibrium models. The contributions of this paper are three-fold.

First, we develop path-conservative central-upwind (PCCU) numerical schemes for hyperbolic traffic flow models based on their non-conservative form as in (1.3). The PCCU schemes were derived in [7] for general 1-D non-conservative hyperbolic systems (1.3). While these schemes are robust and thus applicable to a wide variety of non-conservative system, they are only second-order accurate and this limits their ability to achieve high resolution of certain practically important solutions.

Higher-order PCCU schemes have been recently developed in [12] in the framework of finite-difference alternative weighted essentially non-oscillatory (A-WENO) schemes. Our second contribution is to modify the A-WENO PCCU scheme from [12] and apply the modified scheme to three different traffic models from [65, 70, 71]. The modification is necessary as the schemes from [12] may produce inaccurate and oscillatory results in several important numerical examples. The resulting second- and fifth-order schemes are tested on a number of challenging numerical examples, which clearly show that both schemes are robust and capable of producing quite accurate results. At the same time, the fifth-order A-WENO PCCU scheme produces sharper results in many of the considered numerical examples.

Thirdly, we propose efficient treatments to suppress the inherent numerical oscillations that may potentially arise when WENO-type schemes are applied to nonlinear hyperbolic systems. We emphasize that even though our A-WENO PCCU scheme is based on a very accurate and essentially non-oscillatory WENO-Z interpolation [12, 28, 41, 63] applied to the characteristic fields using the local characteristic decomposition [12, 19, 28, 41, 50, 63], oscillations can still occur. Therefore, in order to suppress these non-physical spurious oscillations, we supplement the developed A-WENO PCCU scheme with the adaptive artificial viscosity (AAV) taken to be proportional to the size of the weak local residual (WLR) as it was proposed in [9, 34] for general hyperbolic systems of conservative laws. We compute the WLR based on the conservative continuity equation, which allows us to directly extend the AAV approach from [9, 34] to the studied non-conservative systems.

The rest of the paper is organized as follows. In Section 2, we briefly describe a second-order finite-volume (FV) PCCU scheme for the non-conservative system (1.4). In Section 3, we construct a new fifth-order A-WENO PCCU scheme. In Section 4, we show how the AAV can be incorporated into the proposed A-WENO PCCU scheme. In Section 5, we present the numerical results. Finally, in Section 6, we give some concluding remarks and comment on the future development and applications of the proposed A-WENO PCCU scheme.

## 2    Second-order FV PCCU schemes: A brief overview

In this section, we consider the non-conservative hyperbolic system (1.4) and review the second-order FV PCCU schemes introduced in [7] and then modified in [12].

Suppose that a numerical solution realized in terms of its cell averages

$$\overline{U}_j(t) :\approx \frac{1}{\Delta x} \int_{C_j} U(x,t)\, dx,$$

is available at a certain time $t$. Here, $C_j := \left(x_{j-\frac{1}{2}}, x_{j+\frac{1}{2}}\right)$ are the cells, which are assumed (for simplicity) to be uniform so that $x_{j+\frac{1}{2}} - x_{j-\frac{1}{2}} \equiv \Delta x$ for all $j$. The cell centers are then given by $x_j = x_{j-\frac{1}{2}} + \Delta x/2$.

The numerical solution is evolved in time by solving the following system of ODEs:

$$\frac{d\overline{U}_j}{dt} = -\frac{1}{\Delta x}\left[ H_{j+\frac{1}{2}} - H_{j-\frac{1}{2}} - B_j - \frac{a_{j-\frac{1}{2}}^+}{a_{j-\frac{1}{2}}^+ - a_{j-\frac{1}{2}}^-} B_{\Psi,j-\frac{1}{2}} + \frac{a_{j+\frac{1}{2}}^-}{a_{j+\frac{1}{2}}^+ - a_{j+\frac{1}{2}}^-} B_{\Psi,j+\frac{1}{2}} \right] + S(U_j), \quad (2.1)$$

which is obtained by applying the semi-discrete PCCU scheme from [12] to the system (1.4). Note that all of the indexed quantities in (2.1) are time-dependent, but from here on we omit this dependence for the sake of brevity. In (2.1),

$$H_{j+\frac{1}{2}} = \frac{a_{j+\frac{1}{2}}^+ F(U_{j+\frac{1}{2}}^-) - a_{j+\frac{1}{2}}^- F(U_{j+\frac{1}{2}}^+)}{a_{j+\frac{1}{2}}^+ - a_{j+\frac{1}{2}}^-} + \frac{a_{j+\frac{1}{2}}^+ a_{j+\frac{1}{2}}^-}{a_{j+\frac{1}{2}}^+ - a_{j+\frac{1}{2}}^-}\left( U_{j+\frac{1}{2}}^+ - U_{j+\frac{1}{2}}^- - Q_{j+\frac{1}{2}} \right) \quad (2.2)$$

are CU numerical fluxes derived in [33]. Here, $U_{j+\frac{1}{2}}^{\pm}$ are the right- and left-sided point values of $U$ at the cell interface $x = x_{j+\frac{1}{2}}$. They are obtained with the help of a conservative piecewise linear reconstruction,

$$\widetilde{U}(x) = \overline{U}_j + (U_x)_j (x - x_j), \quad x \in C_j, \quad (2.3)$$

which gives

$$U_{j+\frac{1}{2}}^- = \overline{U}_j + \frac{\Delta x}{2}(U_x)_j, \quad U_{j+\frac{1}{2}}^+ = \overline{U}_{j+1} - \frac{\Delta x}{2}(U_x)_{j+1}.$$

The slopes $(U_x)_j$ in (2.3) are to be computed using a nonlinear limiter to ensure the non-oscillatory nature of this reconstruction. In all of the numerical experiments reported in Section 5, we have used the minmod limiter (see, e.g., [58]):

$$(U_x)_j = \text{minmod}\left( \frac{\overline{U}_j - \overline{U}_{j-1}}{\Delta x}, \frac{\overline{U}_{j+1} - \overline{U}_j}{\Delta x} \right),$$

applied in the component-wise manner. Here, the minmod function is defined as

$$\text{minmod}(z_1, z_2) := \frac{\text{sign}(z_1) + \text{sign}(z_2)}{2} \cdot \min(|z_1|, |z_2|).$$

Next,

$$Q_{j+\frac{1}{2}} = \text{minmod}\left(U_{j+\frac{1}{2}}^+ - U_{j+\frac{1}{2}}^*, U_{j+\frac{1}{2}}^* - U_{j+\frac{1}{2}}^-\right),$$

where

$$U_{j+\frac{1}{2}}^* = \frac{a_{j+\frac{1}{2}}^+ U_{j+\frac{1}{2}}^+ - a_{j+\frac{1}{2}}^- U_{j+\frac{1}{2}}^- - \left\{F(U_{j+\frac{1}{2}}^+) - F(U_{j+\frac{1}{2}}^-)\right\}}{a_{j+\frac{1}{2}}^+ - a_{j+\frac{1}{2}}^-}$$

is a "built-in" anti-diffusion term in the numerical flux (2.2), and

$$a_{j+\frac{1}{2}}^- = \min\left\{\lambda_1(\mathcal{A}(U_{j+\frac{1}{2}}^+)), \lambda_1(\mathcal{A}(U_{j+\frac{1}{2}}^-)), 0\right\}, \quad a_{j+\frac{1}{2}}^+ = \max\left\{\lambda_N(\mathcal{A}(U_{j+\frac{1}{2}}^+)), \lambda_N(\mathcal{A}(U_{j+\frac{1}{2}}^-)), 0\right\},$$

are estimates of the one-sided local speeds of propagation obtained using the eigenvalues of $\mathcal{A}$: $\lambda_1(\mathcal{A}) \leq \cdots \leq \lambda_N(\mathcal{A})$.

Finally, the terms $B_j$ and $B_{\Psi,j+\frac{1}{2}}$ in (2.1) reflect the contributions of the non-conservative product terms inside the computational cell $C_j$ and at its interface $x_{j+\frac{1}{2}}$, respectively:

$$B_j :\approx \int_{C_j} B(\widetilde{U}(x)) \frac{\mathrm{d}\widetilde{U}(x)}{\mathrm{d}x} \mathrm{d}x, \quad B_{\Psi,j+\frac{1}{2}} :\approx \int_0^1 B(\Psi_{j+\frac{1}{2}}(s)) \frac{\mathrm{d}\Psi_{j+\frac{1}{2}}(s)}{\mathrm{d}s} \mathrm{d}s. \tag{2.4}$$

Here, $\Psi_{j+\frac{1}{2}}(s)$ is a path connecting the left- and right-sided states $U_{j+\frac{1}{2}}^-$ and $U_{j+\frac{1}{2}}^+$ at each cell interface and in this paper, we have used the linear segment path

$$\Psi_{j+\frac{1}{2}}(s) = U_{j+\frac{1}{2}}^- + s(U_{j+\frac{1}{2}}^+ - U_{j+\frac{1}{2}}^-). \tag{2.5}$$

Substituting (2.3) and (2.5) into (2.4) results in

$$B_j \approx \frac{1}{2}\left[B(U_{j-\frac{1}{2}}^+) + B(U_{j+\frac{1}{2}}^-)\right](U_{j+\frac{1}{2}}^- - U_{j-\frac{1}{2}}^+),$$

$$B_{\Psi,j+\frac{1}{2}} \approx \frac{1}{2}\left[B(U_{j+\frac{1}{2}}^-) + B(U_{j+\frac{1}{2}}^+)\right](U_{j+\frac{1}{2}}^+ - U_{j+\frac{1}{2}}^-).$$

## 3  Fifth-order A-WENO finite-difference PCCU schemes

In this section, we extend the second-order FV PCCU scheme reviewed in Section 2 to a fifth-order A-WENO PCCU scheme. We begin along the lines of [12] and rewrite the non-conservative system (1.4) in the following quasi-conservative form:

$$U_t + K(U)_x = S(U), \quad K(U(x,t)) = F(U(x,t)) - \int_{\widehat{x}}^x B(U(\xi,t))U_x(\xi,t)\mathrm{d}\xi, \tag{3.1}$$

where $K$ is a global flux and $\widehat{x}$ is an arbitrary number. The fifth-order A-WENO scheme for the system (3.1) then reads as (see [12])

$$
\frac{\mathrm{d}U_j}{\mathrm{d}t} = -\frac{1}{\Delta x}\left[ H_{j+\frac{1}{2}} - H_{j-\frac{1}{2}} - B_j - \frac{a^+_{j-\frac{1}{2}}}{a^+_{j-\frac{1}{2}} - a^-_{j-\frac{1}{2}}} B_{\Psi,j-\frac{1}{2}} + \frac{a^-_{j+\frac{1}{2}}}{a^+_{j+\frac{1}{2}} - a^-_{j+\frac{1}{2}}} B_{\Psi,j+\frac{1}{2}} \right]
$$
$$
+ \frac{\Delta x}{24}\left[ (K_{xx})_{j+\frac{1}{2}} - (K_{xx})_{j-\frac{1}{2}} \right] - \frac{7}{5760}(\Delta x)^3 \left[ (K_{xxxx})_{j+\frac{1}{2}} - (K_{xxxx})_{j-\frac{1}{2}} \right] + S(U_j). \quad (3.2)
$$

Here, $H_{j+\frac{1}{2}}$, $B_j$, $B_{\Psi,j+\frac{1}{2}}$ and $a^{\pm}_{j+\frac{1}{2}}$ are defined as in Section 2, but with $U^{\pm}_{j+\frac{1}{2}}$ computed using the fifth-order WENO-Z interpolant from [12,28,41,63] applied to the local characteristic variables. The details on the WENO-Z interpolant are prescribed in Appendix A, and the details on the local characteristic decompositions for each of the studied traffic flow systems can be found in Section 5.

Finally, $(K_{xx})_{j+\frac{1}{2}}$ and $(K_{xxxx})_{j+\frac{1}{2}}$ are finite-difference approximations of the second- and fourth-order spatial derivatives of the function $K(U(\cdot,t))$. They can be computed in the way, which was proposed in [12, §4]; namely, using the facts that $K_{xx} = F_{xx} - (B(U)U_x)_x$ and $K_{xxxx} = F_{xxxx} - (B(U)U_x)_{xxx}$. However, the resulting A-WENO scheme would be quite oscillatory when applied to the studied traffic flow models. We therefore propose a new way of evaluating $(K_{xx})_{j+\frac{1}{2}}$ and $(K_{xxxx})_{j+\frac{1}{2}}$. We use the following finite-difference approximations:

$$
(K_{xx})_{j+\frac{1}{2}} = \frac{1}{48(\Delta x)^2}\left( -5K_{j-2} + 39K_{j-1} - 34K_j - 34K_{j+1} + 39K_{j+2} - 5K_{j+3} \right),
$$
$$
(K_{xxxx})_{j+\frac{1}{2}} = \frac{1}{2(\Delta x)^4}\left( K_{j-2} - 3K_{j-1} + 2K_j + 2K_{j+1} - 3K_{j+2} + K_{j+3} \right),
$$

where $K_j = F(U_j) - I_{j-1}$ and

$$
I_j := \approx \int_{x_j}^{x_{j+1}} B(U(\xi,t))U_x(\xi,t)\,\mathrm{d}\xi. \quad (3.3)
$$

In order to obtain a fifth-order numerical scheme, the integral $I_j$ needs to be evaluated at least within the fifth order of accuracy. To this end, we develop a special fifth-order A-WENO quadrature for the integrals in (3.3). Our quadrature is the Newton-Cotes method based on the five points $x_j$, $x_{j+\frac{1}{4}}$, $x_{j+\frac{1}{2}}$, $x_{j+\frac{3}{4}}$ and $x_{j+1}$, and the corresponding values of $U$ at these points: $U_j$, $U_{j+\frac{1}{4}}$, $U_{j+\frac{1}{2}}$, $U_{j+\frac{3}{4}}$ and $U_{j+1}$. Notice that the values $U_j$ and $U_{j+1}$ are given. We then set $U_{j+\frac{1}{2}} = \left( U^-_{j+\frac{1}{2}} + U^+_{j+\frac{1}{2}} \right)/2$ and evaluate $U_{j+\frac{1}{4}}$ and $U_{j+\frac{3}{4}}$ using the WENO-Z interpolant. Here, we show how to compute $U_{j+\frac{1}{4}}$ as $U_{j+\frac{3}{4}}$ can be calculated in the mirror-symmetric way.

For each component of $\boldsymbol{U}_{j+\frac{1}{4}}$, the value $U^{(i)}_{j+\frac{1}{4}}$ is calculated using a weighted average of the three parabolic interpolants $\mathcal{P}^{(i)}_0(x)$, $\mathcal{P}^{(i)}_1(x)$ and $\mathcal{P}^{(i)}_2(x)$ as in (A.1), namely,

$$U^{(i)}_{j+\frac{1}{4}}=\sum_{k=0}^{2}\omega^{(i)}_k\mathcal{P}^{(i)}_k(x_{j+\frac{1}{4}}),$$

where

$$\mathcal{P}^{(i)}_0(x_{j+\frac{1}{4}})=\frac{5}{32}U^{(i)}_{j-2}-\frac{9}{16}U^{(i)}_{j-1}+\frac{45}{32}U^{(i)}_j,$$

$$\mathcal{P}^{(i)}_1(x_{j+\frac{1}{4}})=-\frac{3}{32}U^{(i)}_{j-1}+\frac{15}{16}U^{(i)}_j+\frac{5}{32}U^{(i)}_{j+1},$$

$$\mathcal{P}^{(i)}_2(x_{j+\frac{1}{4}})=\frac{21}{32}U^{(i)}_j+\frac{7}{16}U^{(i)}_{j+1}-\frac{3}{32}U^{(i)}_{j+2},$$

and the weights $\omega^{(i)}_k$ are calculated by (A.2)–(A.4), but with $d_0=7/64$, $d_1=21/32$ and $d_2=15/64$.

Equipped with the point values of $\boldsymbol{U}_k$, $k=j, j+\frac{1}{4}, j+\frac{1}{2}, j+\frac{3}{4}$ and $j+1$, we first construct a fourth-degree interpolating polynomials in the interval $[x_j, x_{j+1}]$. We then use the same interpolation technique to approximate all entries in the matrix $B(\boldsymbol{U})$, and substitute the obtained interpolating polynomials into the integral in (3.3), which is then evaluated exactly.

In order to evaluate $\boldsymbol{I}_j$, we notice that we will need to evaluate integrals of the form $\int_{x_j}^{x_{j+1}}\sigma\phi_x\,\mathrm{d}x$, where $\sigma:=\big(B(\boldsymbol{U})\big)_{m\ell}$ and $\phi:=U^{(\ell)}$. To this end, we take the interpolating polynomial

$$
\begin{aligned}
\widetilde{\sigma}(x)=\frac{1}{3(\Delta x)^4}\Big[&3(\Delta x)^4\sigma_j-(\Delta x)^3\big(25\sigma_j-48\sigma_{j+\frac{1}{4}}+36\sigma_{j+\frac{1}{2}}-16\sigma_{j+\frac{3}{4}}+3\sigma_{j+1}\big)(x-x_j)\\
&+2(\Delta x)^2\big(35\sigma_j-104\sigma_{j+\frac{1}{4}}+114\sigma_{j+\frac{1}{2}}-56\sigma_{j+\frac{3}{4}}+11\sigma_{j+1}\big)(x-x_j)^2\\
&-16\Delta x\big(5\sigma_j-18\sigma_{j+\frac{1}{4}}+24\sigma_{j+\frac{1}{2}}-14\sigma_{j+\frac{3}{4}}+3\sigma_{j+1}\big)(x-x_j)^3\\
&+32\big(\sigma_j-4\sigma_{j+\frac{1}{4}}+6\sigma_{j+\frac{1}{2}}-16\sigma_{j+\frac{3}{4}}+\sigma_{j+1}\big)(x-x_j)^4\Big],\quad x\in[x_j,x_{j+1}],
\end{aligned}
$$

and the derivative of the interpolating polynomial $\widetilde{\phi}_x(x)$, namely,

$$
\begin{aligned}
\widetilde{\phi}_x(x)=\frac{1}{3(\Delta x)^4}\Big[&(\Delta x)^3\big(-25\phi_j+48\phi_{j+\frac{1}{4}}-36\phi_{j+\frac{1}{2}}+16\phi_{j+\frac{3}{4}}-3\phi_{j+1}\big)\\
&+4(\Delta x)^2\big(35\phi_j-104\phi_{j+\frac{1}{4}}+114\phi_{j+\frac{1}{2}}-56\phi_{j+\frac{3}{4}}+11\phi_{j+1}\big)(x-x_j)\\
&-48\Delta x\big(5\phi_j-18\phi_{j+\frac{1}{4}}+24\phi_{j+\frac{1}{2}}-14\phi_{j+\frac{3}{4}}+3\phi_{j+1}\big)(x-x_j)^2\\
&+128\big(\phi_j-4\phi_{j+\frac{1}{4}}+6\phi_{j+\frac{1}{2}}-4\phi_{j+\frac{3}{4}}+\phi_{j+1}\big)(x-x_j)^3\big)\Big],\quad x\in[x_j,x_{j+1}],
\end{aligned}
$$

and then substitute them into $\int_{x_j}^{x_{j+1}} \sigma\phi_x\,\mathrm{d}x$ to obtain

$$
\begin{aligned}
\int\limits_{x_j}^{x_{j+1}} \sigma\phi_x\,\mathrm{d}x \approx \int\limits_{x_j}^{x_{j+1}} \widetilde{\sigma}(x)\widetilde{\phi}_x(x)\,\mathrm{d}x &= \mathcal{Q}(\sigma_j, \sigma_{j+\frac{1}{4}}, \sigma_{j+\frac{1}{2}}, \sigma_{j+\frac{3}{4}}, \sigma_{j+1}, \phi_j, \phi_{j+\frac{1}{4}}, \phi_{j+\frac{1}{2}}, \phi_{j+\frac{3}{4}}, \phi_{j+1}) \\
&:= \frac{1}{1890}\Big[ \sigma_j\big(-945\phi_j + 1472\phi_{j+\frac{1}{4}} - 804\phi_{j+\frac{1}{2}} + 384\phi_{j+\frac{3}{4}} - 107\phi_{j+1}\big) \\
&\quad + \sigma_{j+\frac{1}{4}}\big(-1472\phi_j + 2112\phi_{j+\frac{1}{2}} - 1024\phi_{j+\frac{3}{4}} + 384\phi_{j+1}\big) \\
&\quad + \sigma_{j+\frac{1}{2}}\big(804\phi_j - 2112\phi_{j+\frac{1}{4}} + 2112\phi_{j+\frac{3}{4}} - 804\phi_{j+1}\big) \\
&\quad + \sigma_{j+\frac{3}{4}}\big(-384\phi_j + 1024\phi_{j+\frac{1}{4}} - 2112\phi_{j+\frac{1}{2}} + 1472\phi_{j+1}\big) \\
&\quad + \sigma_{j+1}\big(107\phi_j - 384\phi_{j+\frac{1}{4}} + 804\phi_{j+\frac{1}{2}} - 1472\phi_{j+\frac{3}{4}} + 945\phi_{j+1}\big)\Big].
\end{aligned}
\tag{3.4}
$$

**Remark 3.1.** In order to ensure the designed A-WENO PCCU scheme is fifth-order accurate, the term $B_j$ needs to be evaluated using at least a fifth-order quadrature. In this paper, we use the same Newton-Cotes quadrature $\mathcal{Q}$ as in (3.4), namely,

$$
\int\limits_{C_j} \sigma\phi_x\,\mathrm{d}x \approx \int\limits_{C_j} \widetilde{\sigma}(x)\widetilde{\phi}_x(x)\,\mathrm{d}x = \mathcal{Q}(\sigma_{j-\frac{1}{2}}, \sigma_{j-\frac{1}{4}}, \sigma_j, \sigma_{j+\frac{1}{4}}, \sigma_{j+\frac{1}{2}}, \phi_{j-\frac{1}{2}}, \phi_{j-\frac{1}{4}}, \phi_j, \phi_{j+\frac{1}{4}}, \phi_{j+\frac{1}{2}}).
$$

# 4 Adaptive artificial viscosity (AAV)

The fifth-order A-WENO PCCU scheme presented in Section 3 is essentially non-oscillatory. However, in some situations the so-called WENO-type oscillations may appear and they may be quite large. Recent studies [44, 45] have found that numerical oscillations particularly arise when high-order schemes are applied to the class of non-equilibrium continuum models devoid of source terms (see, e.g., [70]), which are studied in this paper (see Section 5.3). In order to suppress these oscillations, we propose to add a certain amount of the AAV within the A-WENO framework. This results in the following A-WENO PCCU scheme with the AAV (compare with (3.2)):

$$
\begin{aligned}
\frac{\mathrm{d}U_j}{\mathrm{d}t} = &-\frac{1}{\Delta x}\left[ H_{j+\frac{1}{2}} - H_{j-\frac{1}{2}} - B_j - \frac{a_{j-\frac{1}{2}}^+}{a_{j-\frac{1}{2}}^+ - a_{j-\frac{1}{2}}^-} B_{\Psi,j-\frac{1}{2}} + \frac{a_{j+\frac{1}{2}}^-}{a_{j+\frac{1}{2}}^+ - a_{j+\frac{1}{2}}^-} B_{\Psi,j+\frac{1}{2}} \right] \\
&+ \frac{\Delta x}{24}\left[ (K_{xx})_{j+\frac{1}{2}} - (K_{xx})_{j-\frac{1}{2}} \right] - \frac{7}{5760}(\Delta x)^3\left[ (K_{xxxx})_{j+\frac{1}{2}} - (K_{xxxx})_{j-\frac{1}{2}} \right] + S(U_j) \tag{4.1} \\
&+ \mu \frac{\varepsilon_{j+\frac{1}{2}}(U_{j+1} - U_j) - \varepsilon_{j-\frac{1}{2}}(U_j - U_{j-1})}{(\Delta x)^2}. \tag{4.2}
\end{aligned}
$$

Here, $\mu$ is a positive constant and $\varepsilon_{j+\frac{1}{2}}:=|E_{j+\frac{1}{2}}(t)|$, where $E_{j+\frac{1}{2}}(t)$ is the WLR (which was derived in [34]) computed based on the conservative continuity equation $\rho_t+(\rho V)_x=0$:

$$
\begin{aligned}
E_{j+\frac{1}{2}}(t)=\frac{\Delta x}{6}&\left[\rho_{j+\frac{3}{2}}(t)-\rho_{j+\frac{3}{2}}(t-\Delta t)+4\big(\rho_{j+\frac{1}{2}}(t)-\rho_{j+\frac{1}{2}}(t-\Delta t)\big)+\rho_{j-\frac{1}{2}}(t)-\rho_{j-\frac{1}{2}}(t-\Delta t)\right]\\
&+\frac{\Delta t}{4}\left[(\rho V)_{j+\frac{3}{2}}(t)-(\rho V)_{j-\frac{1}{2}}(t)+(\rho V)_{j+\frac{3}{2}}(t-\Delta t)-(\rho V)_{j-\frac{1}{2}}(t-\Delta t)\right],\qquad(4.3)
\end{aligned}
$$

where $\rho_{j+\frac{1}{2}}:=\big(\rho_{j+\frac{1}{2}}^-+\rho_{j+\frac{1}{2}}^+\big)/2$ and $(\rho V)_{j+\frac{1}{2}}:=\big[(\rho V)_{j+\frac{1}{2}}^-+(\rho V)_{j+\frac{1}{2}}^+\big]/2$.

The constant $\mu$ is to be selected for each problem at hand. As suggested in [9,34], we tune $\mu$ on a coarse mesh and then use the same value of $\mu$ on finer meshes. We note that in most examples considered in Section 5, we have used $\mu=0$ as the A-WENO PCCU scheme from Section 3 typically does not generate large oscillations.

We note that adding the AAV on the RHS of (4.1) affects the formal order of accuracy of the semi-discrete A-WENO scheme. Indeed, substituting a smooth exact solution satisfying $\rho_t+(\rho V)_x=0$ into (4.3) and using the Taylor expansion about $(x_{j+\frac{1}{2}},t-\frac{\Delta t}{2})$ result in

$$
E_{j+\frac{1}{2}}(t)=-\frac{1}{12}\Delta x(\Delta t)^3\rho_{ttt}+\mathcal{O}\big(\Delta x(\Delta t)^5\big)+\mathcal{O}\big((\Delta x)^3(\Delta t)^3\big)+\mathcal{O}\big((\Delta x)^5\Delta t\big).\qquad(4.4)
$$

At the same time, the magnitude of the WLR near shocks is $\mathcal{O}(\Delta x)+\mathcal{O}(\Delta t)$, which is sufficiently large to suppress most of the oscillations appearing in the vicinities of shocks.

Based on (4.4), one can conclude that the formal order of accuracy of the resulting fully discrete scheme based on the semi-discretization (4.1) depends on the accuracy of the ODE solver used for the time discretization. In all of the numerical examples reported in Section 5, we have used the three-stage third-order strong stability preserving (SSP) Runge-Kutta method (see, e.g., [21,22]), which is commonly used due to its high efficiency combined with very good stability properties, both the linear and nonlinear ones. Therefore, the size of the local truncation error of the resulting fully discrete scheme becomes

$$
\mathcal{O}\big((\Delta x)^5\big)+\mathcal{O}\big((\Delta t)^3\big)+\mathcal{O}\big(\Delta x(\Delta t)^3\big),\qquad(4.5)
$$

which means that adding the AAV does not reduce the formal order of accuracy of the proposed A-WENO scheme. If a higher-order ODE solver is utilized, then the use of the WLR (4.3) will reduce the order. In order to prevent the order reduction, (4.3) can be replaced with a higher-order WLR (introduced in [31,32]), which is based on the data computed on three consecutive time levels rather than the two levels used in (4.3).

# 5   Non-equilibrium traffic flow models in the non-conservative form: Numerical tests and discussion

In this section, we implement the proposed numerical scheme on various non-equilibrium traffic flow models. We test the proposed fifth-order A-WENO PCCU

scheme on several numerical examples and compare its performances with the corresponding second-order FV PCCU scheme. The tested schemes will be referred to as the 5-Order Scheme and 2-Order Scheme, respectively.

In all of the examples, we use the CFL number 0.5 and impose free boundary conditions since our primary focus is on Riemann problems at homogeneous sections of freeways and not the boundary conditions at junctions. In most cases, where the structure of solutions is well-known, we only present the results for the traffic density to save space. Wherever applicable, we also present the results for the traffic speed to supplement the theoretical discussions.

## 5.1  The Aw-Rascle-Zhang model in the non-conservative form

In the first example, we consider the Aw-Rascle-Zhang (ARZ) model introduced in [3,70]. We emphasize that this model can be written in the conservative form as:

$$\begin{cases} \rho_t + (\rho V(\rho,\omega))_x = 0, \\ \omega_t + (\omega V(\rho,\omega))_x = 0, \end{cases} \tag{5.1}$$

where $\omega := \rho(V - V_e(\rho))$ describes the deviation of traffic flow from the "equilibrium" state. Characteristic speeds in the ARZ model are

$$\lambda_1 = V + C(\rho) \quad \text{and} \quad \lambda_2 = V, \tag{5.2}$$

where $C(\rho) = \rho V_e'(\rho)$ is the propagation speed of smooth variations in traffic density from the perspective of the LWR model (1.1).

Even though the ARZ model is conservative and thus can be solved by numerical methods for hyperbolic systems of conservation laws, we consider the ARZ model and solve it in both conservative and non-conservative forms for several reasons:

(1) to showcase our proposed numerical scheme for capturing solution structures against well-established benchmarks. Note that the existence of global entropic weak solutions were proved for the ARZ model in [1], and its analytic solutions were obtained in [36,42];

(2) to demonstrate the robustness of the proposed schemes as high-order numerical methods often exhibit spurious oscillations around intermediate states, such as those connecting shocks and contact discontinuities; see [44,45];

(3) due to strong potentials of the ARZ model to accommodate complex human psychological factors. This model can be viewed as a hydrodynamic limit of stimulus-response car-following models [2], where drivers' response time is a simplified function of available spacing. The stimulus-response models can be easily extended to incorporate complex human psychological factors (e.g., risk perception, perception errors), in which case, the resulting continuum models are likely to be non-conservative.

We now discuss the specifications for the numerical experiments. The function $V_e(\rho)$ in (5.1) is adopted as

$$V_e(\rho) = V_{\max}\left(1 - \frac{\rho}{\rho_{\max}}\right), \tag{5.3}$$

where $\rho_{\max}$ and $V_{\max}$ are constants representing the maximum density and speed, respectively. For all of the numerical tests in this example, we choose $\rho_{\max} = 0.18 \, veh/m$ and $V_{\max} = 30 \, m/s$ from the typical range as in [44]. While the function in (5.3) is inadequate with respect to empirical observations [43], it results in well-known analytic solutions. With respect to (5.3), the field that corresponds to $\lambda_1$ in (5.2) is genuinely nonlinear in the entire density domain $(0, \rho_{\max}]$ and can produce shock waves in deceleration (referred to as H1) or rarefaction waves in acceleration (referred to as R1). On the other hand, the field that corresponds to $\lambda_2$ is linearly degenerate and can only produce contact discontinuities (referred to as C2 waves).

The conservative system (5.1), (5.3) can be viewed as the system (1.4) with $B(\boldsymbol{U}) = \boldsymbol{0}$ and $S(\boldsymbol{U}) = \boldsymbol{0}$. Thus, we compute its numerical solutions using the fifth-order A-WENO scheme presented in Section 3, but with $\boldsymbol{B}_j = \boldsymbol{0}$, $\boldsymbol{B}_{\boldsymbol{\Psi}, j+\frac{1}{2}} = \boldsymbol{0}$ and $S(\boldsymbol{U}_j) = \boldsymbol{0}$. In order to implement the proposed numerical scheme, we rewrite the conservative system (5.1), (5.3) in the non-conservative form as

$$\begin{cases} \rho_t + (\rho V)_x = 0, \\ V_t + \left(\dfrac{V^2}{2}\right)_x = -C(\rho)V_x, \end{cases} \tag{5.4}$$

where

$$C(\rho) = \rho V_e'(\rho) = -\frac{V_{\max}}{\rho_{\max}}\rho. \tag{5.5}$$

As mentioned in Section 3, we apply the WENO-Z interpolation procedure to the local characteristic variables, which are obtained using the local characteristic decomposition. This is carried out as follows. We first use the notation

$$\boldsymbol{U} = \begin{pmatrix} \rho \\ V \end{pmatrix}, \quad \boldsymbol{F}(\boldsymbol{U}) = \begin{pmatrix} \rho V \\ \dfrac{V^2}{2} \end{pmatrix}, \quad B(\boldsymbol{U}) = \begin{pmatrix} 0 & 0 \\ 0 & -C \end{pmatrix},$$

and then introduce

$$\mathcal{A}_{j+\frac{1}{2}} = A\big(\widehat{\boldsymbol{U}}_{j+\frac{1}{2}}\big) - B\big(\widehat{\boldsymbol{U}}_{j+\frac{1}{2}}\big) = \begin{pmatrix} \widehat{V}_{j+\frac{1}{2}} & \widehat{\rho}_{j+\frac{1}{2}} \\ 0 & \widehat{C}_{j+\frac{1}{2}} + \widehat{V}_{j+\frac{1}{2}} \end{pmatrix},$$

where, as before, $A = \frac{\partial \boldsymbol{F}}{\partial \boldsymbol{u}}$, and $\widehat{\rho}_{j+\frac{1}{2}}$ and $\widehat{V}_{j+\frac{1}{2}}$ stand for the following Roe averages:

$$\widehat{\rho}_{j+\frac{1}{2}} = \frac{\rho_j + \rho_{j+1}}{2}, \quad \widehat{V}_{j+\frac{1}{2}} = \frac{\sqrt{\rho_j}V_j + \sqrt{\rho_{j+1}}V_{j+1}}{\sqrt{\rho_j} + \sqrt{\rho_{j+1}}}, \quad \widehat{C}_{j+\frac{1}{2}} = -\frac{V_{\max}}{\rho_{\max}}\widehat{\rho}_{j+\frac{1}{2}}. \tag{5.6}$$

We can then compute the matrices

$$R_{j+\frac{1}{2}} = \begin{pmatrix} 1 & \dfrac{\widehat{\rho}_{j+\frac{1}{2}}}{\widehat{C}_{j+\frac{1}{2}}} \\ 0 & 1 \end{pmatrix}, \quad R_{j+\frac{1}{2}}^{-1} = \begin{pmatrix} 1 & -\dfrac{\widehat{\rho}_{j+\frac{1}{2}}}{\widehat{C}_{j+\frac{1}{2}}} \\ 0 & 1 \end{pmatrix},$$

such that $R_{j+\frac{1}{2}}^{-1} \widehat{A}_{j+\frac{1}{2}} R_{j+\frac{1}{2}}$ is a diagonal matrix, and introduce the local characteristic variables in the neighborhood of $x = x_{j+\frac{1}{2}}$:

$$\Gamma_k = R_{j+\frac{1}{2}}^{-1} U_k, \quad k = j-2, \cdots, j+3.$$

Finally, we apply the WENO-Z interpolation to these six values of $\Gamma$, obtain the point values $\Gamma_{j+\frac{1}{2}}^{\pm}$, and then end up with

$$U_{j+\frac{1}{2}}^{\pm} = R_{j+\frac{1}{2}} \Gamma_{j+\frac{1}{2}}^{\pm}.$$

**Remark 5.1.** The local characteristic decomposition for the conservative system (5.1), (5.3) can be performed in a similar manner.

Equipped with the reconstructed values of $\rho_{j+\frac{1}{2}}^{\pm}$ and $V_{j+\frac{1}{2}}^{\pm}$, we estimate the one-sided local speeds of propagation as follows:

$$a_{j+\frac{1}{2}}^{+} = \max\left\{ V_{j+\frac{1}{2}}^{+}, V_{j+\frac{1}{2}}^{-}, 0 \right\}, \quad a_{j+\frac{1}{2}}^{-} = \min\left\{ V_{j+\frac{1}{2}}^{+} + C_{j+\frac{1}{2}}^{+}, V_{j+\frac{1}{2}}^{-} + C_{j+\frac{1}{2}}^{-}, 0 \right\},$$

where $C_{j+\frac{1}{2}}^{\pm} = -\dfrac{V_{\max}}{\rho_{\max}} \rho_{j+\frac{1}{2}}^{\pm}$.

### 5.1.1 Accuracy test

First, we consider the following smooth initial data:

$$\rho(x,0) = \begin{cases} \rho_{\max}\left(1 + \frac{1}{10}\sin^4\left(\frac{\pi}{24000}(x-8000)\right)\right), & 8000 < x < 32000, \\ \rho_{\max}, & \text{otherwise,} \end{cases}$$

$$V(x,0) = \begin{cases} V_{\max}\left(1 + \frac{1}{10}\sin^4\left(\frac{\pi}{24000}(x-8000)\right)\right), & 8000 < x < 32000, \\ V_{\max}, & \text{otherwise,} \end{cases}$$

in the computational domain $[0,40000]$ subject to free boundary conditions. We compute the numerical solution until the final time $t = 20s$ (at which the solution is still smooth; see Fig. 1) using the 5-Order scheme with and without the added AAV (when it is added, the parameter $\mu = 100$) on a sequence of uniform meshes with $\Delta x = 5, 5/2, 5/4,$ and $5/8$. We then compute the $L^1$-errors and estimate the experimental convergence rates using the following Runge formulae, which are based on the solutions computed on the three
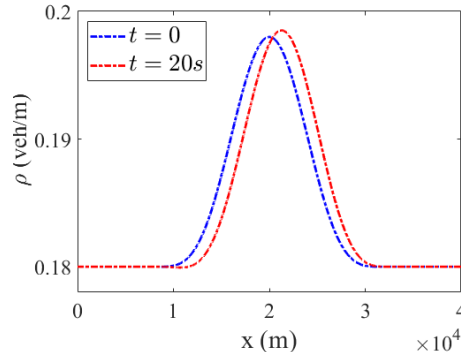
Figure 1: ARZ model, accuracy test: Density ($\rho$) profiles at $t=0$ and $20s$ computed by the New 5-Order scheme.

Table 1: Accuracy test: $L^1$-errors and experimental convergence rates for the density ($\rho$).

| | $\Delta t \sim (\Delta x)$ | | | | $\Delta t \sim \Delta x^{5/3}$ | | | |
| $\Delta x$ | Without AAV | | With AAV | | Without AAV | | With AAV | |
| | Error | Rate | Error | Rate | Error | Rate | Error | Rate |
| 5/4 | 1.57e-8 | 3.04 | 1.57e-8 | 3.04 | 4.72e-8 | 4.96 | 4.68e-8 | 4.95 |
| 5/8 | 1.92e-9 | 2.94 | 1.92e-9 | 2.94 | 1.52e-9 | 4.82 | 1.52e-9 | 4.82 |

consecutive uniform grids with the mesh sizes $\Delta x$, $2\Delta x$, and $4\Delta x$ and denoted by $(\cdot)^{\Delta x}$, $(\cdot)^{2\Delta x}$, and $(\cdot)^{4\Delta x}$, respectively:

$$\text{Error}(\Delta x) \approx \frac{\delta_{24}^2}{|\delta_{12} - \delta_{24}|}, \quad \text{Rate}(\Delta x) \approx \log_2\left(\frac{\delta_{24}}{\delta_{12}}\right).$$

Here, $\delta_{12} := \|(\cdot)^{\Delta x} - (\cdot)^{2\Delta x}\|_{L^1}$ and $\delta_{24} := \|(\cdot)^{2\Delta x} - (\cdot)^{4\Delta x}\|_{L^1}$.

We first perform the computations using the timestep size $\Delta t \sim \Delta x$, which is selected based on the stability requirement. The obtained results reported in Table 1 clearly demonstrate that in this case, as expected according to (4.5), the temporal error dominates and the convergence rate is the third one. We then select $\Delta t \sim \Delta x^{5/3}$, which balances the contribution of the temporal and spatial errors in (4.5), and then the fifth order of accuracy is achieved; see Table 1. We would also like to stress that adding the AAV practically does not affect the size of the error.

### 5.1.2 Riemann problems

We now consider several Riemann initial data of the form

$$\boldsymbol{U}(x,0) = \begin{cases} \boldsymbol{U}_L, & \text{if } x < x_0, \\ \boldsymbol{U}_R, & \text{otherwise,} \end{cases} \tag{5.7}$$

and begin with the illustration of importance of the new way the terms $(\boldsymbol{K}_{xx})_{j+\frac{1}{2}}$ and $(\boldsymbol{K}_{xxxx})_{j+\frac{1}{2}}$ are computed. Recall that in Section 3, we have introduced a new finite-

Table 2: ARZ model: Initial conditions for Tests 1 and 2.

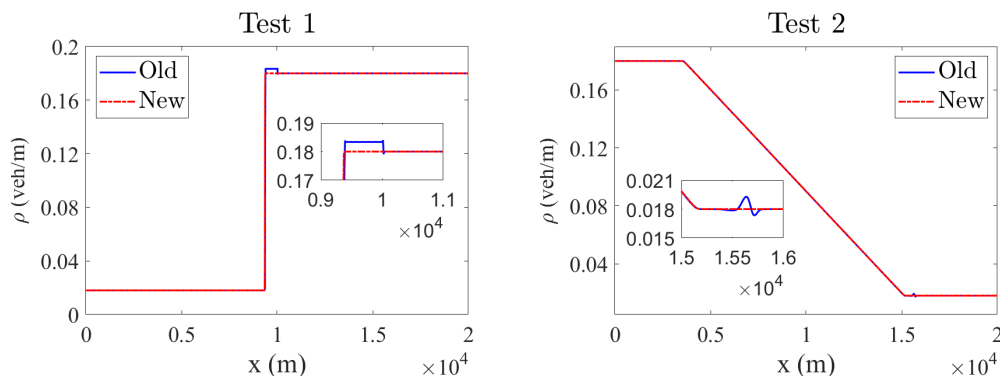| Test | $\rho_L$ | $\rho_R$ | $V_L$ | $V_R$ | $x_0$ |
|------|----------|----------|-------|-------|-------|
| 1 | 0.018 | 0.18 | 28.8 | 0 | 10000 |
| 2 | 0.18 | 0.018 | 0 | 28.8 | 10000 |



Figure 2: ARZ model: Density ($\rho$) profiles at $t=200s$ computed by the New and Old 5-Order schemes for Tests 1 and 2.

difference approximations of these terms (New 5-Order Scheme), which is different compared with the way these terms were evaluated in [12, §4] (Old 5-Order Scheme).

We consider Tests 1 and 2, which correspond to the data provided in Table 2. We compute the corresponding solutions of the non-conservative system (5.4)-(5.5) on the computational domain $[0,20000]$ using 2000 uniform cells until the final time $t=200s$ and present the numerical results computed by the New and Old 5-Order Schemes in Fig. 2. As one can see, in Test 1, the Old 5-Order Scheme produces an artificial plateau to the right of the shock wave and in Test 2, the Old 5-Order Scheme generates non-physical oscillations to the right of the rarefaction corner. Therefore, from here on, we will use only the New 5-Order Scheme, which will be referred as the 5-Order Scheme.

We now apply the 5-Order and 2-Order Schemes to both the conservative (5.1), (5.3) and non-conservative (5.4)-(5.5) systems. Our goal is to demonstrate that the "conservative" and "non-conservative" results are about the same. To this end, we design additional numerical tests according to the scenarios presented in Table 3, which cover a comprehensive range of Riemann problems for different traffic regimes. In all of the tests, a "non-equilibrium" state with $V \neq V_e(\rho)$ reaches an "equilibrium" state with $V = V_e(\rho)$ from behind. In all of the tests, $\lambda_2$ consists of C2 waves which always travel downstream; see, e.g., [42, 44] for more elaborations.

Tests 3–5 describe situations, where traffic states are faster in the upstream, so that $\lambda_1$ produces H1 shocks. For both Tests 3 and 4, an intermediate states, which connects the H1 shocks on the left to C2 waves on the right. For Test 3, shock wave travels downstream because of the free-flow traffic, whereas it travels upstream in Test 4, which describes

Table 3: ARZ model: Initial conditions for Tests 3–8.

| Test | $\rho_L$ | $\rho_R$ | $V_L$ | $V_R$ | $x_0$ |
|---|---|---|---|---|---|
| 3 | $0.3\rho_{\max}$ | $0.3\rho_{\max}$ | $V_e(\rho)+5$ | $V_e(\rho)$ | 20000 |
| 4 | $0.7\rho_{\max}$ | $0.3\rho_{\max}$ | $V_e(\rho)+5$ | $V_e(\rho)$ | 20000 |
| 5 | $0.4\rho_{\max}$ | $0.7\rho_{\max}$ | $V_e(\rho)+5$ | $V_e(\rho)$ | 20000 |
| 6 | $0.3\rho_{\max}$ | $0.3\rho_{\max}$ | $V_e(\rho)-5$ | $V_e(\rho)$ | 20000 |
| 7 | $0.7\rho_{\max}$ | $0.7\rho_{\max}$ | $V_e(\rho)-5$ | $V_e(\rho)$ | 20000 |
| 8 | $0.7\rho_{\max}$ | $0.4\rho_{\max}$ | $V_e(\rho)-5$ | $V_e(\rho)$ | 20000 |

a congestion condition. Test 5 includes a more complex scenario, where a strong H1 shock occurs because a near-capacity free-flow condition in the upstream meets a highly congested downstream state.

Tests 6–8 describe situations, where traffic condition on the left-hand side of the initial discontinuity is slower than that on the right-hand side. In all of these tests, $\lambda_1$ generates R1 acceleration waves, which are separated from the contact discontinuity by an intermediate state. The rarefaction wave travels downstream in Test 6, due to the free-flow condition, whereas it travels upstream in Test 7, due to the congested states. Test 9 involves a more complex case, where due to transition from the congested to free-flow states, the rarefaction wave travels both in the upstream and downstream directions.

From a numerical perspective, the tests in Table 3 present two challenging aspects of the ARZ model. First, it is well-established that contact discontinuities are difficult to capture and that high-order numerical schemes can still exhibit substantial diffusion around such waves. Second, in the case of the ARZ model, high-order schemes (e.g., WENO-type schemes) often become oscillatory around intermediate states [44].

Let us now discuss the performance of the proposed A-WENO PCCU scheme in capturing the solution structures for the tests in Table 3. To this end, we compute the solutions on the computational domain [0,40000] using 200 uniform cells until the final time $t = 200s$. The numerical results obtained by solving the conservative (5.1), (5.3) and non-conservative (5.4)-(5.5) systems are shown in Figs. 3 and 4 together with the reference solution computed by 5-Order Scheme on a very fine mesh with 40000 uniform cells. As one can see, the obtained "conservative" and "non-conservative" results are very close. This demonstrates the efficacy of our proposed path-conservative approach in capturing the solution structures in the Riemann problems.

Furthermore, in all of the tests, the proposed A-WENO PCCU scheme performs robustly and accurately. For instance, the 5-Order Scheme substantially suppresses the numerical diffusion around contact discontinuities and achieves higher resolutions especially in Tests 3 and 6.

Another aspect worth discussing is how the proposed A-WENO PCCU scheme performs in capturing the intermediate states. By visually comparing the "conservative" and "non-conservative" results, one can spot some WENO-inherent oscillations in both
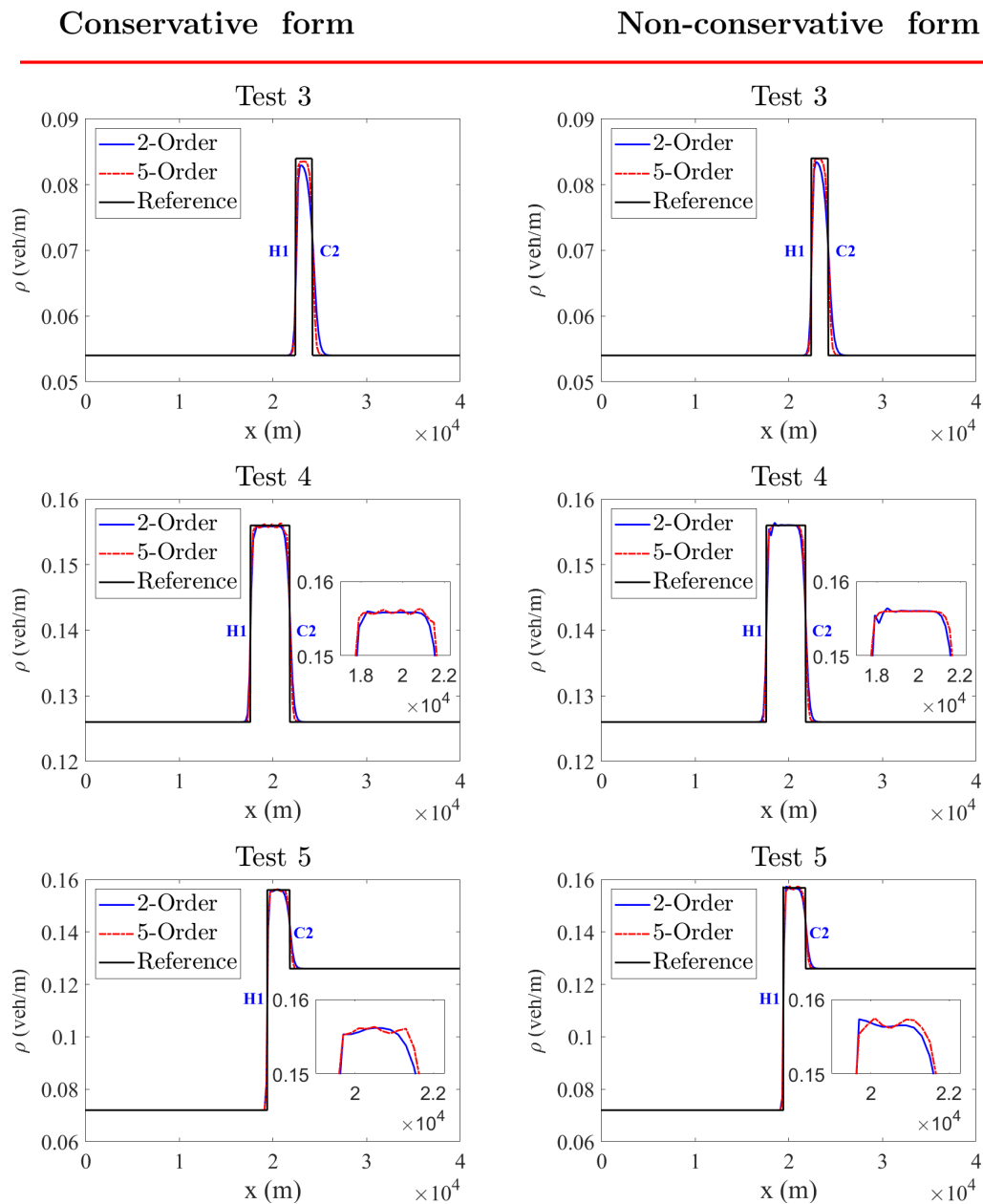
Figure 3: ARZ model, Tests 3–5: Density ($\rho$) profiles at $t = 200s$ computed by solving the conservative (left column) and non-conservative (right column) systems.

cases. However, the observed oscillations are overall low-amplitude in all tests, and interestingly, for some tests, such as Test 7, the use of the path-conservative technique in the "non-conservative" computations suppresses the oscillations more effectively. The slight

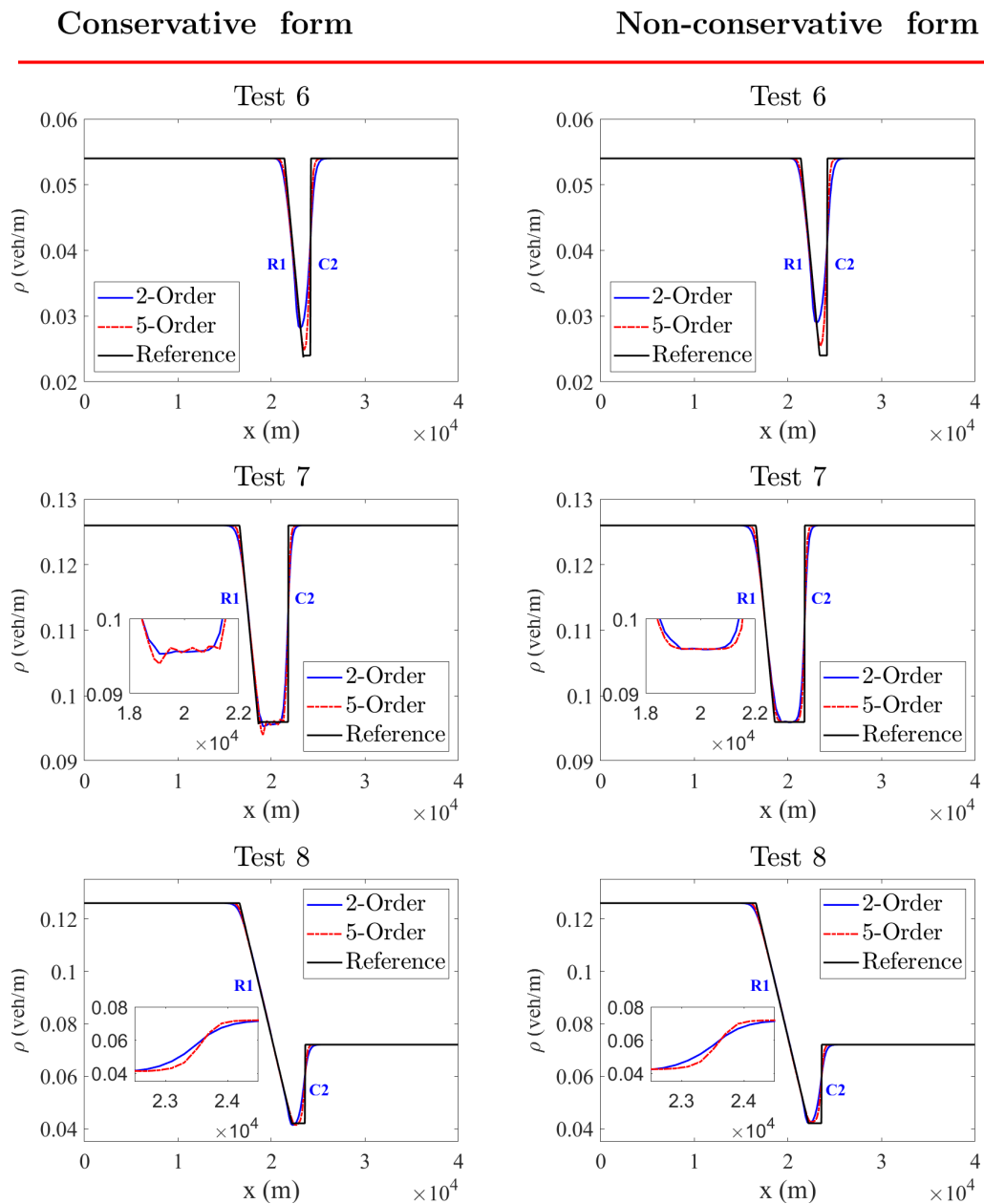**Conservative  form**                    **Non-conservative  form**



Figure 4: ARZ model, Tests 6–8: Same as in Fig. 3.

oscillations around the intermediate states further decrease in magnitude when the mesh is refined; see the reference solutions. Note that we have deliberately selected a coarse mesh size with $\Delta x = 200m$ for practical purposes. We also emphasize that we did not need to use the AAV to suppress the numerical oscillations in any of the considered tests.

**Conservative  form**                                    **Non-conservative  form**
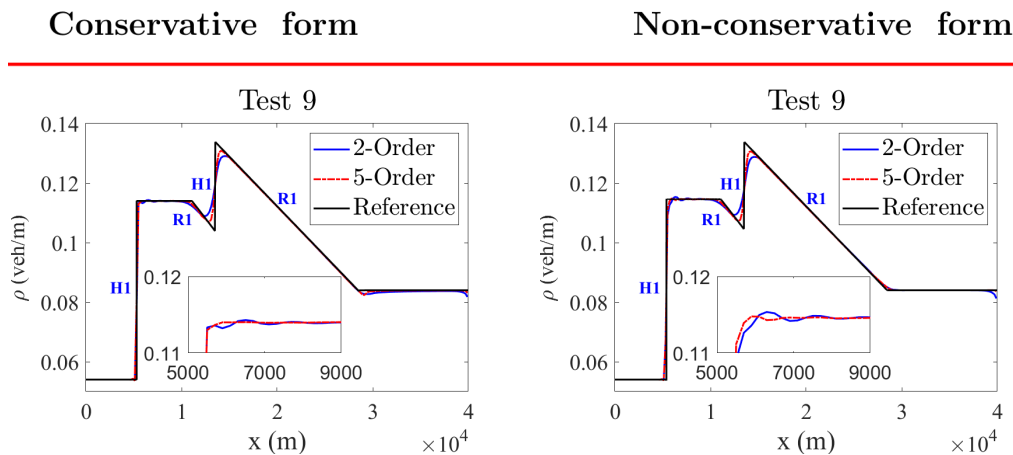


Figure 5: ARZ model, Test 9: Same as in Figs. 3 and 4.

In order to further elaborate on this point, we consider another intricate numerical example with the following initial data:

$$\rho(x,0) = \begin{cases} 0.3\rho_{\max}, & 0 < x < 8000, \\ 0.8\rho_{\max}, & 8000 \le x < \dfrac{80000}{3}, \\ 0.3\rho_{\max}, & \text{otherwise}, \end{cases} \quad V(x,0) = \begin{cases} 0.3V_e(\rho) - 5, & 0 < x < 8000, \\ 0.8V_e(\rho), & 8000 \le x < \dfrac{80000}{3}, \\ 0.3V_e(\rho) - 5, & \text{otherwise}. \end{cases}$$

This numerical example has been recently studied in [44], and the findings there suggested that a combination of the WENO-Z reconstruction and HLL-type numerical fluxes can produce strong oscillatory behavior near the intermediate states. Using the same parameter set-up, we study this numerical example using the same computational domain $[0,40000]$, take 200 uniform cells, and compute the solutions until the final time $t = 900s$. The obtained results, plotted in Fig. 5 together with the reference solutions computed by the 5-Order Scheme using 40000 uniform cells, clearly demonstrate the robustness of the "non-conservative" scheme, and also show that the 5-Order Scheme outperforms the 2-Order Scheme.

This section was primarily focused around showcasing the proposed A-WENO PCCU scheme's performance, where our benchmarking ARZ model was originally presented in the conservative form and we have artificially rewritten it in the non-conservative way. In the following, we test the PCCU numerical schemes on generally non-conservative behavioral non-equilibrium models.

## 5.2  The behavioral 1998 Zhang model in the non-conservative form

In this section, we consider the behavioral non-equilibrium traffic model proposed by Zhang in 1998 in [65]. This model has been derived from an improved car-following

relation, in which driver's reaction delay is explicitly incorporated. The non-conservative form of this model is

$$\begin{cases} \rho_t + (\rho V)_x = 0, \\ V_t + \left(\dfrac{V^2}{2}\right)_x = -\dfrac{C^2(\rho)}{\rho}\rho_x + \dfrac{1}{\tau}(V_e(\rho) - V), \end{cases} \tag{5.8}$$

where $C(\rho) = \rho V'_e(\rho) \leq 0$ is the so-called "sonic" velocity and $\tau$ is the relaxation time.

The 1998 Zhang model has two characteristic speeds:

$$\lambda_1 = V + C(\rho) \quad \text{and} \quad \lambda_2 = V - C(\rho).$$

From a theoretical perspective, the model admits the condition $\lambda_2 > V$, meaning that traffic waves can reach vehicles from behind and affect their dynamics, and thereby violating the anisotropy property of traffic flow; see, e.g., [14,72]. However, this behavioral model still has promising potentials with regard to complex aspects of traffic flow such as traffic instabilities [66].

In [68], a generic conservative form has been proposed for the 1998 Zhang model:

$$\begin{cases} \rho_t + (\rho V)_x = 0, \\ V_t + \dfrac{1}{2}\left(V^2 + \mathcal{F}(\rho)\right)_x = \dfrac{1}{\tau}(V_e(\rho) - V), \end{cases} \tag{5.9}$$

where $\mathcal{F}'(\rho) = \rho(V'_e(\rho))^2$. However, depending on the choice of $V_e(\rho)$, the function $\mathcal{F}(\rho)$ may not be specified in closed from, thereby hindering the application of conservative numerical schemes.

Our primary focus in this section is to demonstrate the performance of the proposed A-WENO PCCU scheme for this behavioral model. To this end, we restrict our consideration to a simplified case by choosing the function $V_e(\rho)$ as in (5.3) which results in $\mathcal{F}(\rho) = C^2(\rho)$. In this case, the conservative form in (5.9) is specified, and the solution structures are well-documented in [65]. Such a variant of the 1998 Zhang model provides a good benchmark for evaluating our results obtained using the proposed path-conservative approach. In addition, we set $\tau = \infty$ to study the model in the absence of the relaxation term, primarily focusing on capturing the waves propagating with the characteristic speeds. Note that the infinite relaxation time also makes our problem setting more challenging from a numerical perspective since numerical studies on non-equilibrium traffic flow models suggest that relaxation terms can have smoothing effects on spurious oscillations that may arise around the intermediate states [44,45].

We now discuss the specifications of the numerical tests. Similar to the previous case, we choose $\rho_{\max} = 0.18 veh/m$ and $V_{\max} = 30 m/s$, and design comprehensive numerical tests, incorporating all major wave types arising in the solutions of Riemann problems. With the adopted $V_e(\rho)$ as in (5.3), both characteristic fields are genuinely nonlinear in the

Table 4: The 1998 Zhang model: Initial conditions for Tests 1–4.

| Test | $\rho_L$ | $\rho_R$ | $V_L$ | $V_R$ | $x_0$ |
|------|----------|----------|-------|-------|-------|
| 1 | $0.5\rho_{\max}$ | $0.1\rho_{\max}$ | $V_e(\rho)$ | $V_e(\rho)+5$ | 20000 |
| 2 | $0.5\rho_{\max}$ | $0.1\rho_{\max}$ | $V_e(\rho)$ | $V_e(\rho)-5$ | 20000 |
| 3 | $0.3\rho_{\max}$ | $0.7\rho_{\max}$ | $V_e(\rho)$ | $V_e(\rho)-5$ | 20000 |
| 4 | $0.5\rho_{\max}$ | $0.9\rho_{\max}$ | $V_e(\rho)$ | $V_e(\rho)+5$ | 20000 |

entire solution domain, leading to the production of shock and rarefaction waves only. Shock and rarefaction waves corresponding to $\lambda_1$ (H1 and R1, respectively) arise when drivers have to adapt their speed with respect to the traffic conditions ahead. In contrast, shock and rarefaction waves corresponding to $\lambda_2$ (H2 and R2, respectively) reach vehicles from behind and force them to speed up or slow down, respectively. In [68], an analytical framework that divided the $\rho V$-phase plane into four regions associated with each wave type has been developed. Following this framework, we design a comprehensive set ob numerical tests presented in Table 4.

All of the tests presented in Table 4 describe situations, where "equilibrium" traffic on the left side of the initial discontinuity meets a "non-equilibrium" state on the right side. In all of the cases, one intermediate state arises. In Tests 1 and 2, traffic is heavier in the upstream, and thus $\lambda_1$ produces R1 waves as drivers accelerate to adapt their speed to the lighter traffic ahead. However, the wave types associated with $\lambda_2$ differ in the Tests 1 and 2. In Test 1, the downstream traffic speed is faster than the "equilibrium" one, and thereby $\lambda_2$ produces R2 waves and causes the downstream vehicles to slow down. In Test 2, the downstream traffic speed is slower than the "equilibrium" one, and therefore $\lambda_2$ produces H2 shocks, forcing the downstream vehicles to speed up. Similarly, in both Tests 3 and 4, traffic is lighter in the upstream, and therefore $\lambda_1$ produces H1 shocks for vehicles in the upstream, causing them to sharply decelerate. For Test 3, traffic is slower than the "equilibrium" speed in the downstream, and therefore $\lambda_2$ produces R2 waves forcing the downstream vehicles to slow down, whereas $\lambda_2$ produces H2 waves in Test 4 and force drivers in the downstream to speed up their slower than the "equilibrium" speed.

We emphasize that R2 and H2 waves in the 1998 Zhang model are only occasionally observable in real-world traffic [72]. However, such waves are challenging and interesting cases from a numerical perspective, which is the focus of this paper.

Let us now provide some specifications on the numerical treatments of the state variables. As before, we apply the WENO-Z interpolation procedure to the local characteristic variables for evaluating the point values $\boldsymbol{U}^{\pm}_{j+\frac{1}{2}} = (\rho^{\pm}_{j+\frac{1}{2}}, V^{\pm}_{j+\frac{1}{2}})^{\top}$. We use the same local characteristic decomposition procedure described in Example 1 but with the different

$\mathcal{A}_{j+\frac{1}{2}}$, $R_{j+\frac{1}{2}}$ and $R^{-1}_{j+\frac{1}{2}}$:

$$\mathcal{A}_{j+\frac{1}{2}} = \begin{pmatrix} \widehat{V}_{j+\frac{1}{2}} & \widehat{\rho}_{j+\frac{1}{2}} \\ \dfrac{\widehat{C}^2_{j+\frac{1}{2}}}{\widehat{\rho}_{j+\frac{1}{2}}} & \widehat{V}_{j+\frac{1}{2}} \end{pmatrix}, \quad R_{j+\frac{1}{2}} = \begin{pmatrix} \dfrac{\widehat{\rho}_{j+\frac{1}{2}}}{\widehat{C}_{j+\frac{1}{2}}} & -\dfrac{\widehat{\rho}_{j+\frac{1}{2}}}{\widehat{C}_{j+\frac{1}{2}}} \\ 1 & 1 \end{pmatrix}, \quad R^{-1}_{j+\frac{1}{2}} = \begin{pmatrix} \dfrac{\widehat{C}_{j+\frac{1}{2}}}{2\widehat{\rho}_{j+\frac{1}{2}}} & \dfrac{1}{2} \\ -\dfrac{\widehat{C}_{j+\frac{1}{2}}}{2\widehat{\rho}_{j+\frac{1}{2}}} & \dfrac{1}{2} \end{pmatrix},$$

where $\widehat{\rho}_{j+\frac{1}{2}}$, $\widehat{V}_{j+\frac{1}{2}}$ and $\widehat{C}_{j+\frac{1}{2}}$ are given by (5.6).

Equipped with the reconstructed values of $\rho^{\pm}_{j+\frac{1}{2}}$ and $V^{\pm}_{j+\frac{1}{2}}$, the one-sided local speeds of propagation can be evaluated as follows:

$$a^+_{j+\frac{1}{2}} = \max\left\{V^+_{j+\frac{1}{2}} - C^+_{j+\frac{1}{2}}, V^-_{j+\frac{1}{2}} - C^-_{j+\frac{1}{2}}, 0\right\}, \quad a^-_{j+\frac{1}{2}} = \min\left\{V^+_{j+\frac{1}{2}} + C^+_{j+\frac{1}{2}}, V^-_{j+\frac{1}{2}} + C^-_{j+\frac{1}{2}}, 0\right\}.$$

We now apply the 5-Order and 2-Order Schemes to both the non-conservative (5.8) and conservative (5.9) systems subject to the Riemann initial data (5.7) with the parameters corresponding to Tests 1–4; see Table 4. We compute the numerical solutions on the computational domain [0,40000] using 200 uniform cells until the final time $t = 200s$. The numerical results are presented in Fig. 6 together with the reference solution computed by 5-Order Scheme on a very fine mesh with 40000 uniform cells. These results demonstrate the robust performance of the proposed PCCU schemes in several regards. First, the structure of the solutions and arising waves are captured correctly. As one can clearly see, the "conservative" and "non-conservative" results are almost identical and the 5-Order Scheme achieves higher resolution compared with the 2-Order Scheme, especially in Test 1. One can also observe that the proposed 5-Order Scheme performs very sharply near the H1 and H2 shocks, and it captures the intermediate states quite accurately. As in the case of the ARZ model, one can observe small WENO-type oscillations only and hence there is no need to add the AAV for the 1998 Zhang model as well.

## 5.3   The non-conservative behavioral 2003 Zhang model

In the previous sections, we have tested the proposed PCCU schemes on two non-equilibrium traffic flow models, for which the conservative form was known and analytic solutions were well-documented [42, 68]. By considering such models as benchmarks, we have demonstrated that the proposed A-WENO PCCU scheme performs robustly regarding capturing solution structures, achieving sharp resolution of discontinuities, and suppressing the oscillations around intermediate states.

In this section, we consider a more complicated behavioral non-equilibrium model proposed by Zhang in 2003 in [71]. This model is derived from a car-following relation in which driver memory is explicitly incorporated. The resulting continuum 2003 Zhang
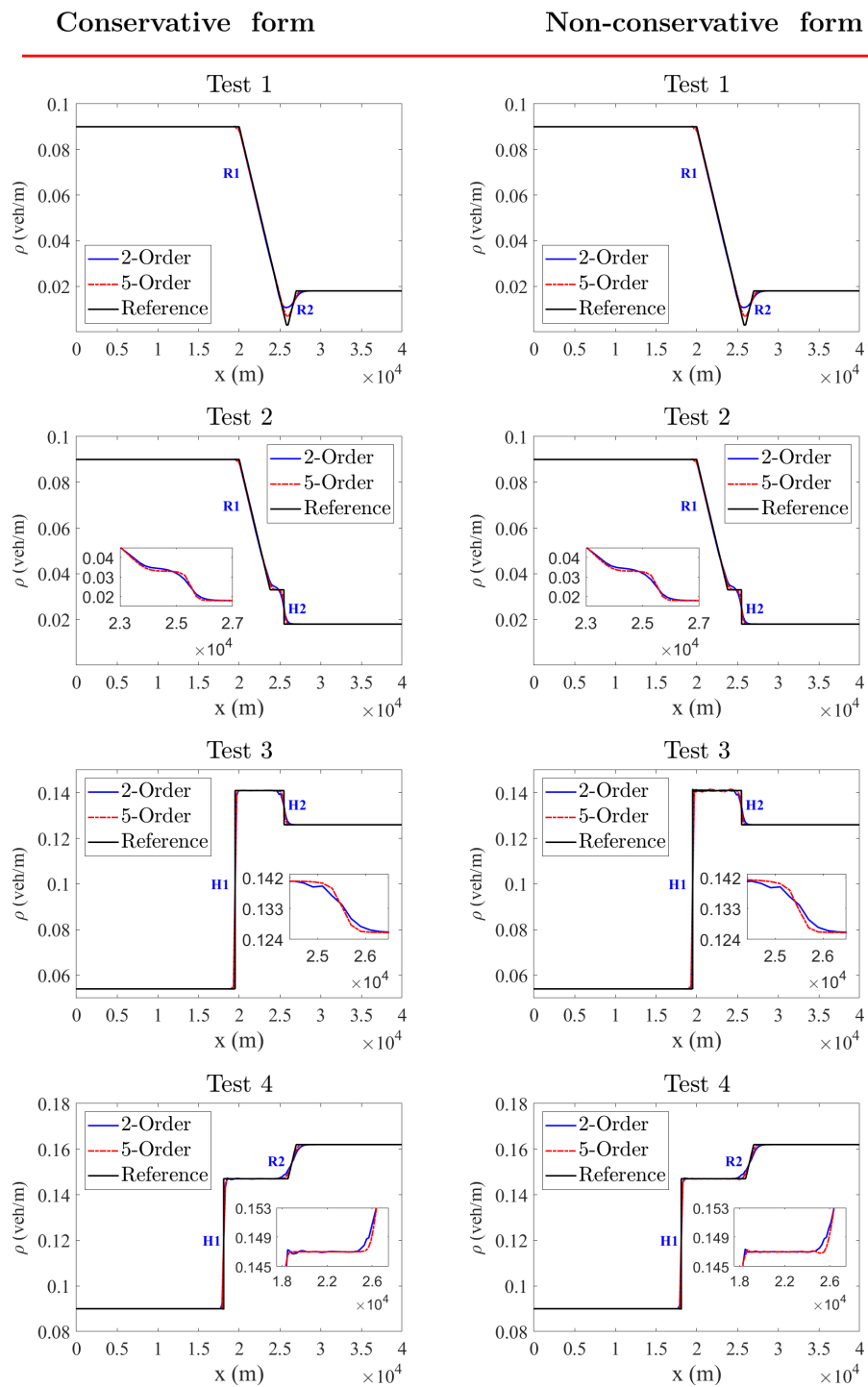
## Conservative form                Non-conservative form



Figure 6: The 1998 Zhang model: Density ($\rho$) profiles at $t = 200s$ computed by solving the conservative (left column) and non-conservative (right column) systems.

model is generically non-conservative and it reads as

$$
\begin{cases}
\rho_t + (\rho V)_x = 0, \\
V_t + \left(\dfrac{V^2}{2}\right)_x = -2\beta C(\rho)V_x - \dfrac{C^2(\rho)}{\rho}\rho_x + \dfrac{1}{\tau}(V_e(\rho) - V) + 2\beta\tau C^2(\rho)V_{xx}.
\end{cases}
\tag{5.10}
$$

Here, $C(\rho) = \rho V_e'(\rho)$, $\beta$ is a constant related to the "driver memory", and $\tau$ is the relaxation time. It is easy to verify that the characteristic speeds of the system (5.10) are

$$
\lambda_1 = V + \left(\beta + \sqrt{1+\beta^2}\right)C(\rho) \quad \text{and} \quad \lambda_2 = V + \left(\beta - \sqrt{1+\beta^2}\right)C(\rho).
\tag{5.11}
$$

Except for very simplified cases (for instance, when $V_e(\rho)$ is linear), the model (5.10) cannot be rewritten in the conservative form. However, linear $V_e(\rho)$ is not realistic and in this section, we consider a robust and well-defined $V_e(\rho)$ given by (see [18]):

$$
V_e(\rho) = \dfrac{C_{\text{jam}}}{\widetilde{\rho}}\left[1 + (a-1)\widetilde{\rho} - \left((a\widetilde{\rho})^\theta + (1-\widetilde{\rho})^\theta\right)^{\frac{1}{\theta}}\right],
\tag{5.12}
$$

where $\widetilde{\rho} = \rho/\rho_{\max}$, $a = V_{\max}/C_{\text{jam}}$, $C_{\text{jam}}$ is the magnitude of the propagation velocity $V_e(\rho) + C(\rho)$ under the jam condition $\rho = \rho_{\max}$, and $\theta > 1$ is a shape parameter. In all of the numerical tests below, we choose $\rho_{\max} = 0.18\,veh/m$, $V_{\max} = 30\,m/s$, $C_{\text{jam}} = 7\,m/s$ from a typical range. The parameter $\theta$ will be selected based on our analytical investigations of this model.

The functional form in (5.12) has numerous promising properties with respect to behavioral aspects of real-world traffic and empirical observations (see, e.g., [43] for more elaborations), which can also make the traffic model (5.10) behaviorally more relevant. However, the complicated nonlinear structure of such $V_e(\rho)$ results in the loss of the conservative form for the model (5.10).

To the best of our knowledge, the 2003 Zhang model has never been studied numerically or analytically. In order to investigate the structure of characteristic waves, we consider the right eigenvectors corresponding to the characteristic speeds (5.11). It is easy to check that they are

$$
r_1(\rho, V) = \left(1, \left(\beta + \sqrt{1+\beta^2}\right)\dfrac{C(\rho)}{\rho}\right)^\top \quad \text{and} \quad r_2(\rho, V) = \left(1, \left(\beta - \sqrt{1+\beta^2}\right)\dfrac{C(\rho)}{\rho}\right)^\top.
\tag{5.13}
$$

Next, from (5.11) and (5.13), we compute

$$
\nabla\lambda_1 \cdot r_1 = \left(\beta + \sqrt{1+\beta^2}\right)\eta(\rho), \ \nabla\lambda_2 \cdot r_2 = \left(\beta - \sqrt{1+\beta^2}\right)\eta(\rho), \ \eta(\rho) := C'(\rho) + \dfrac{C(\rho)}{\rho},
\tag{5.14}
$$

which imply that both characteristic fields are genuinely nonlinear since $\eta(\rho) \neq 0$ for all $\rho \in (0, \rho_{\max})$ and for any finite $\theta$. We plot the function $\eta(\rho)$ for $\theta = 3, 6, 9, \cdots, 30$ in Fig. 7. As
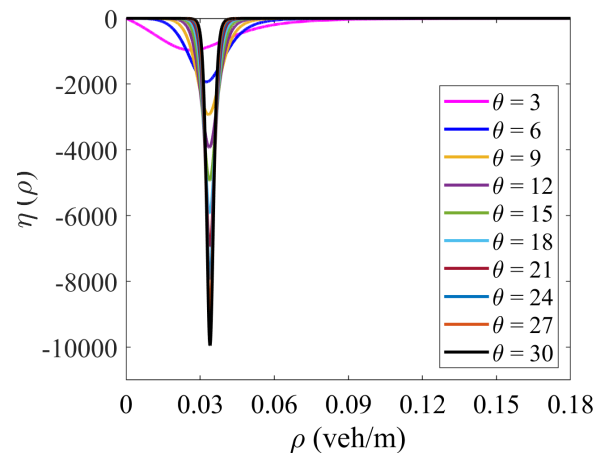
Figure 7: $\eta(\rho) = C'(\rho) + C(\rho)/\rho$ for different $\theta$.

Table 5: The 2003 Zhang model: Initial conditions for Tests 1–4.

| Test | $\rho_L$ | $\rho_R$ | $V_L$ | $V_R$ | $x_0$ |
|------|----------|----------|-------|-------|-------|
| 1 | $0.2\rho_{\max}$ | $0.45\rho_{\max}$ | $V_e(\rho)$ | $V_e(\rho)-5$ | 20000 |
| 2 | $0.2\rho_{\max}$ | $0.8\rho_{\max}$ | $V_e(\rho)$ | $V_e(\rho)+5$ | 20000 |
| 3 | $0.9\rho_{\max}$ | $0.1\rho_{\max}$ | $V_e(\rho)$ | $V_e(\rho)+5$ | 20000 |
| 4 | $0.9\rho_{\max}$ | $0.1\rho_{\max}$ | $V_e(\rho)$ | $V_e(\rho)-5$ | 20000 |

one can see, when $\theta$ is large the values of $|\eta|$ may be very small outside a certain interval $(\rho_1, \rho_2)$. For instance, for $\theta = 15$, $|\eta(\rho)| < 10^{-8}$ for $\rho < \rho_1 \approx 0.0057$ and $\rho > \rho_2 \approx 0.0616$. This means that for any practical purposes the solution of the 2003 Zhang model will behave like a solution of a non-strictly hyperbolic system in the areas where $|\eta|$ rapidly decays. In the numerical experiments presented below, we use $\theta = 3$, for which $|\eta(\rho)|$ is not small near $\rho = 0$ and decays only for larger values of $\rho$.

We design several challenging numerical tests which are presented in Table 5. Similar to the examples considered in previous sections, in all of the cases, "equilibrium" traffic on the left of the initial discontinuity meets a "non-equilibrium" state on the right. However, for the 2003 Zhang model, Riemann solutions depend on several factors (besides the structure of $\lambda_1$ and $\lambda_2$) such as the choice of parameter $\beta$ as well as the diffusion and relaxation terms.

**Case A.** In order to investigate the capability of the proposed A-WENO PCCU scheme to accurately capture the waves arising due to the characteristic speeds, we first consider the system (5.10) in the absence of diffusion and relaxation terms. In this case, the system

reads as

$$\begin{cases} \rho_t + (\rho V)_x = 0, \\ V_t + \left( \dfrac{V^2}{2} \right)_x = -2\beta C(\rho) V_x - \dfrac{C^2(\rho)}{\rho} \rho_x. \end{cases}$$

The point values $U_{j+\frac{1}{2}}^{\pm} = (\rho_{j+\frac{1}{2}}^{\pm}, V_{j+\frac{1}{2}}^{\pm})^{\top}$ will be obtained using the local characteristic decomposition. To this end, we specify $\mathcal{A}_{j+\frac{1}{2}}$, $R_{j+\frac{1}{2}}$ and $R_{j+\frac{1}{2}}^{-1}$ as

$$\mathcal{A}_{j+\frac{1}{2}} = \begin{pmatrix} \widehat{V}_{j+\frac{1}{2}} & \widehat{\rho}_{j+\frac{1}{2}} \\ \dfrac{\widehat{C}_{j+\frac{1}{2}}^2}{\widehat{\rho}_{j+\frac{1}{2}}} & \widehat{V}_{j+\frac{1}{2}} + 2\beta\widehat{C}_{j+\frac{1}{2}} \end{pmatrix}, \quad R_{j+\frac{1}{2}} = \begin{pmatrix} \dfrac{\widehat{\rho}_{j+\frac{1}{2}}}{\widehat{C}_{j+\frac{1}{2}}} \left(\sqrt{1+\beta^2}-\beta\right) & -\dfrac{\widehat{\rho}_{j+\frac{1}{2}}}{\widehat{C}_{j+\frac{1}{2}}} \left(\sqrt{1+\beta^2}+\beta\right) \\ 1 & 1 \end{pmatrix},$$

$$R_{j+\frac{1}{2}}^{-1} = \frac{1}{2\sqrt{1+\beta^2}} \begin{pmatrix} \dfrac{\widehat{C}_{j+\frac{1}{2}}}{\widehat{\rho}_{j+\frac{1}{2}}} & \sqrt{1+\beta^2}+\beta \\ -\dfrac{\widehat{C}_{j+\frac{1}{2}}}{\widehat{\rho}_{j+\frac{1}{2}}} & \sqrt{1+\beta^2}-\beta \end{pmatrix}.$$

The one-sided local speeds of propagation are estimated by

$$a_{j+\frac{1}{2}}^+ = \max\left\{ V_{j+\frac{1}{2}}^+ + \left(\beta - \sqrt{1+\beta^2}\right)C_{j+\frac{1}{2}}^+, V_{j+\frac{1}{2}}^- + \left(\beta - \sqrt{1+\beta^2}\right)C_{j+\frac{1}{2}}^-, 0 \right\},$$

$$a_{j+\frac{1}{2}}^- = \min\left\{ V_{j+\frac{1}{2}}^+ + \left(\beta + \sqrt{1+\beta^2}\right)C_{j+\frac{1}{2}}^+, V_{j+\frac{1}{2}}^- + \left(\beta + \sqrt{1+\beta^2}\right)C_{j+\frac{1}{2}}^-, 0 \right\},$$

where $C_{j+\frac{1}{2}}^{\pm} = \rho_{j+\frac{1}{2}}^{\pm} V_e'\left(\rho_{j+\frac{1}{2}}^{\pm}\right)$.

Next, we numerically solve the system (5.10) using the Riemann initial data (5.7) for different tests in Table 5. The solutions are computed using both the 5-Order and 2-Order Schemes on the computational domain $[0,40000]$ until the final time $t=200s$. We first focus on Tests 1 and 2, which are especially challenging regarding the intermediate states. In Figs. 8 and 9, we present the numerical results computed by the 5-Order Scheme using 200, 400 and 800 uniform cells with $\beta=0$ and 0.2. As one can see, when no AAV is added, that is, when $\mu=0$ in (4.1), the computed solutions contain large oscillations, which do not seem to decay when the mesh is refined. In order to suppress these oscillations, we add the AAV, that is, we take $\mu>0$ in (4.1). As in [9,34], the values of $\mu$ are tuned on the coarse mesh with 200 cells and then the same values are used on finer meshes. In Test 1, we take $\mu=3000$ and 1500 for $\beta=0$ and 0.2, respectively. In Test 2, the corresponding values of $\mu$ are 1500 and 800. One can observe that the use of the AAV helps to significantly reduce the oscillations, whose magnitude substantially decreases when the mesh is refined. We note that in Tests 3 and 4, there is no need to add the AAV as rarefaction waves are dominant and shocks are not as strong.
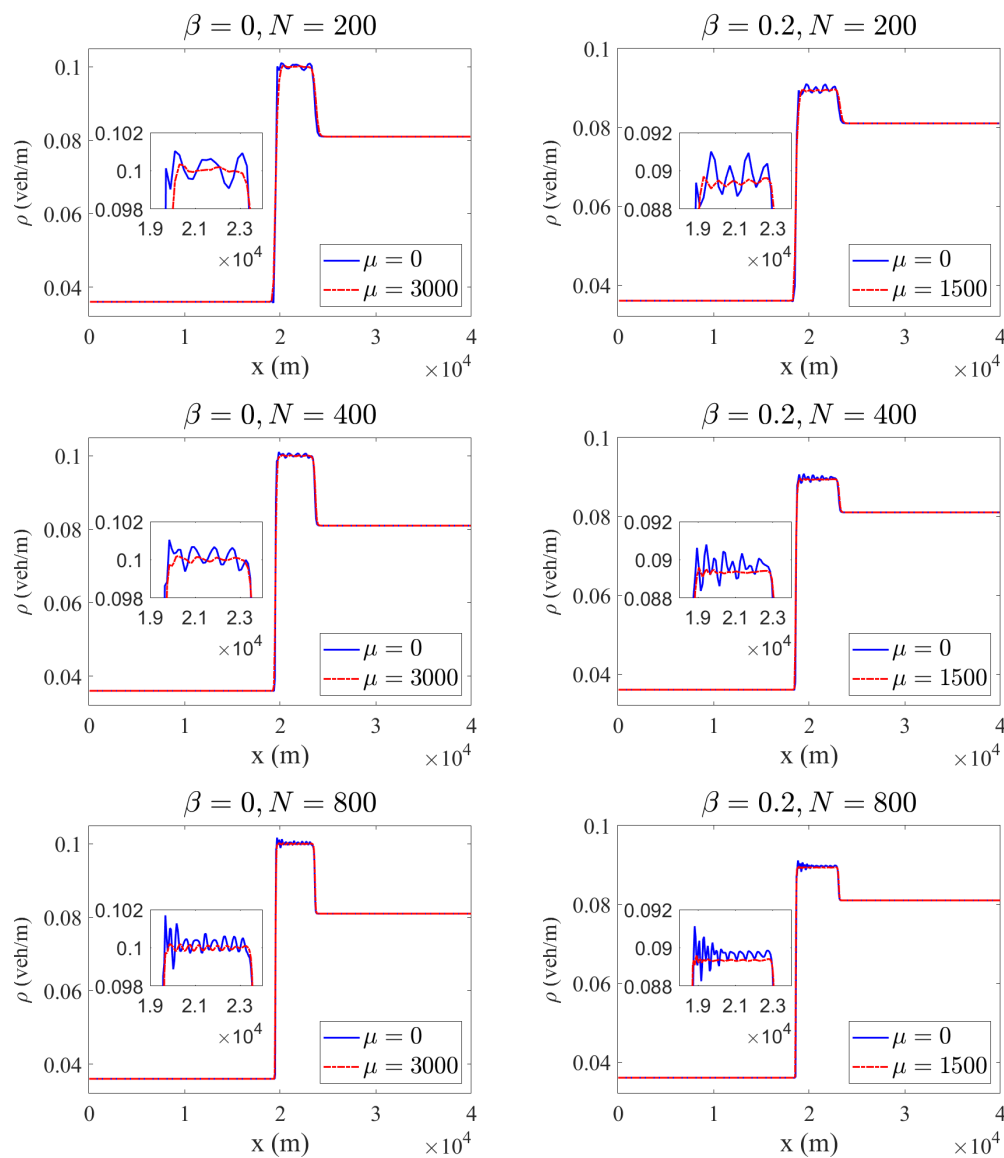
Figure 8: The 2003 Zhang model, Case A, Test 1: Density ($\rho$) profiles at $t = 200s$ computed by the 5-Order Scheme with the AAV parameter $\mu$ (if $\mu = 0$ then the AAV is switched off). The computations have been conducted for $\beta = 0$ (left column) and 0.2 (right column) on three different uniform meshes with 200 (top row), 400 (middle row) and 800 (bottom row) cells.

We then compute the solutions of Tests 1–4 with $\beta = 0$, 0.2, 0.6 and 1 by the 5-Order Scheme using 200 uniform cells and present the obtained results (both $\rho$ and $V$) in Figs. 10-13 together with the corresponding reference solutions computed by the 5-Order Scheme on a finer mesh with 4000 uniform cells. As one can see, the proposed scheme achieves high resolution in all of the tests.
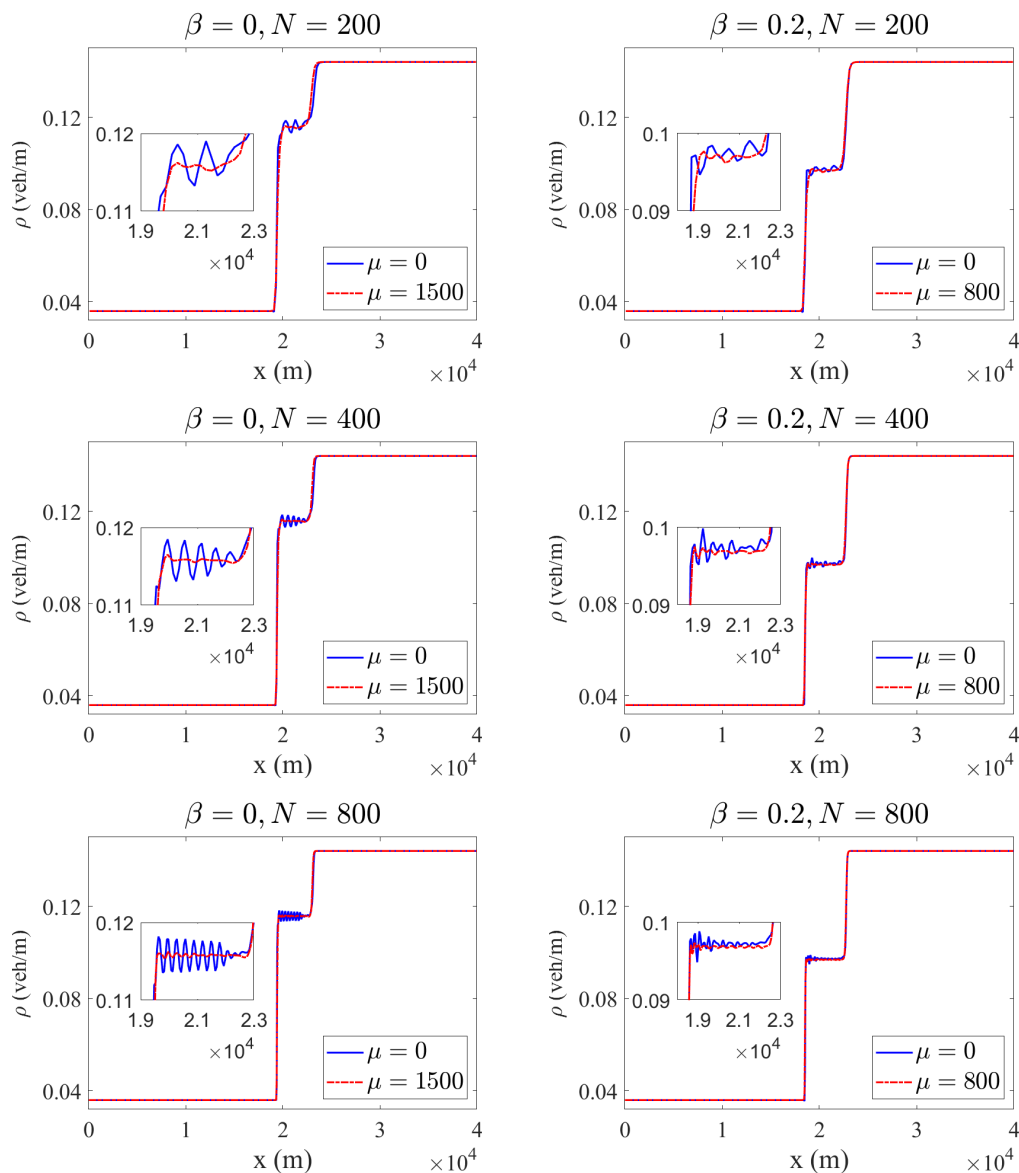
Figure 9: The 2003 Zhang model, Case A, Test 2: Same as in Fig. 8.

We now examine the obtained numerical results based on an analytical considerations. According to the eigenstructure given in (5.11), (5.13) and (5.14), one expects the waves that correspond to $\lambda_1$ and $\lambda_2$ (1- and 2-waves) to be both shock and rarefaction waves for relatively small values of $\rho$, that is, in the area of "effective" support of $\eta(\rho)$, while only shock waves are expected to arise when $\rho$ is large. We consider the results for both density and velocity profiles at $t = 200s$; see Figs. 10-13.
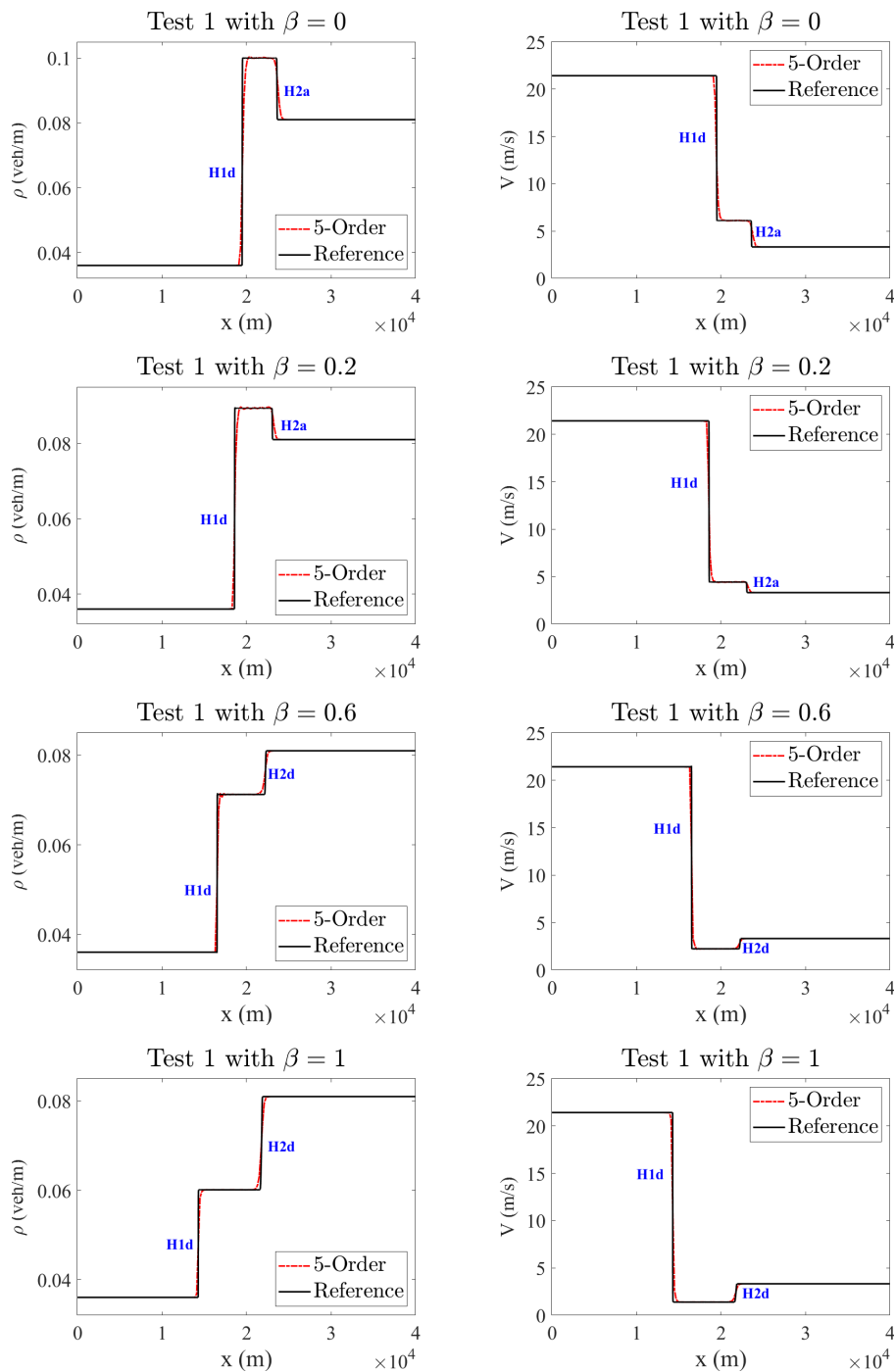
Figure 10: The 2003 Zhang model, Case A, Test 1: Density ($\rho$) and velocity ($V$) profiles at $t=200s$ computed by the 5-Order Scheme. The computations have been conducted for $\beta=0$ (first row), 0.2 (second row), 0.6 (third row) and 1 (fourth row).
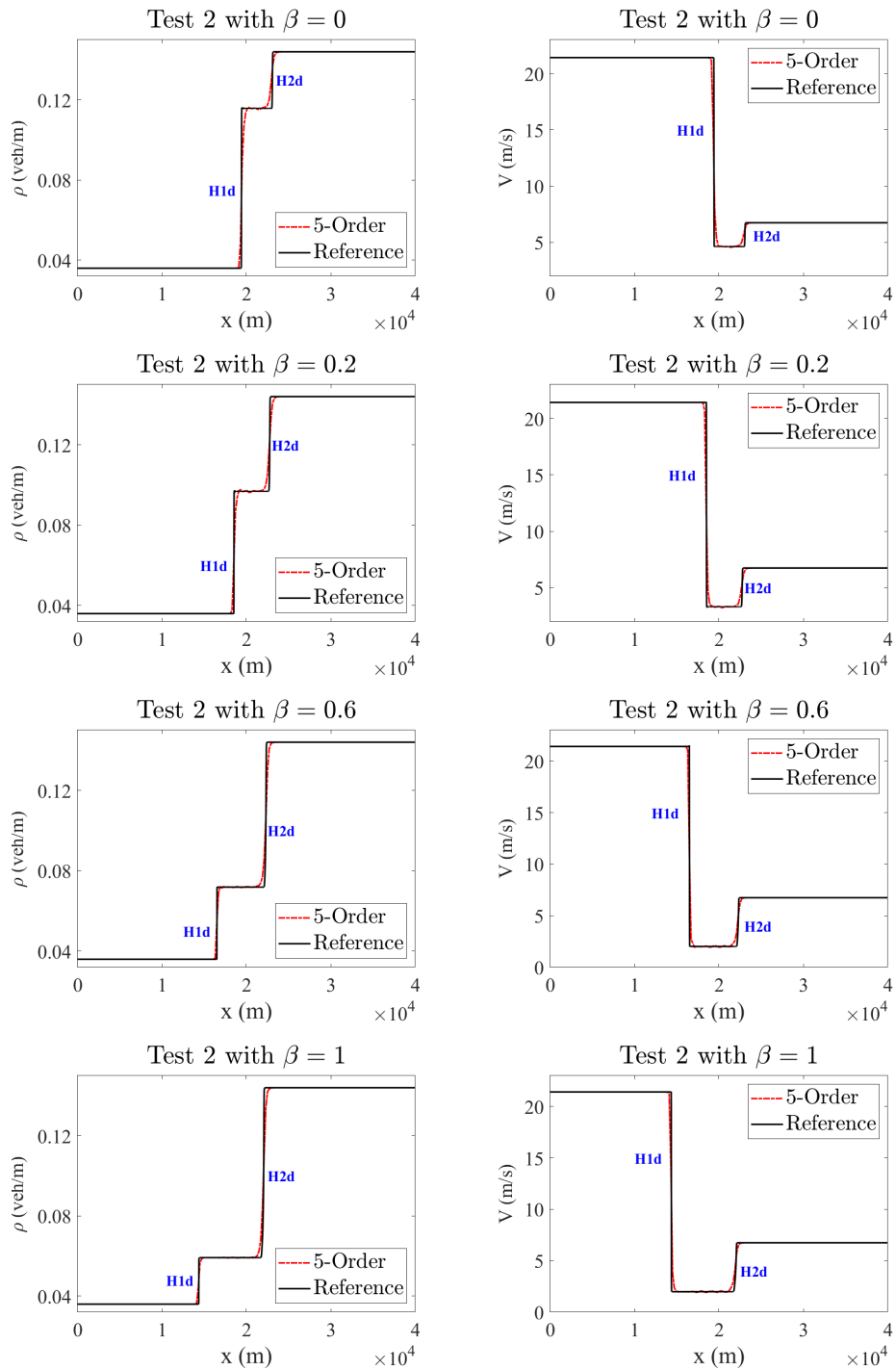
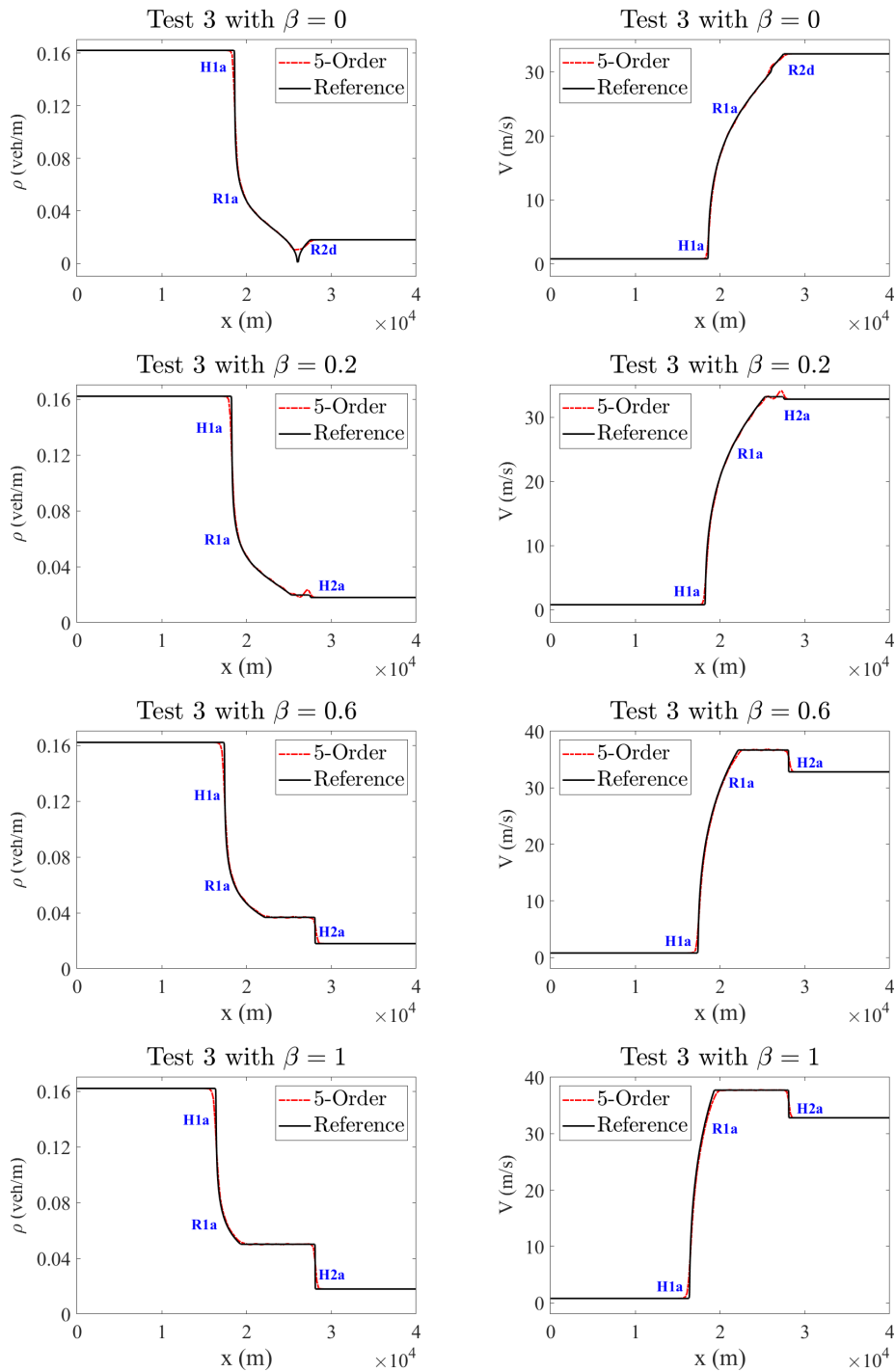Figure 11: The 2003 Zhang model, Case A, Test 2: Same as in Fig. 10.

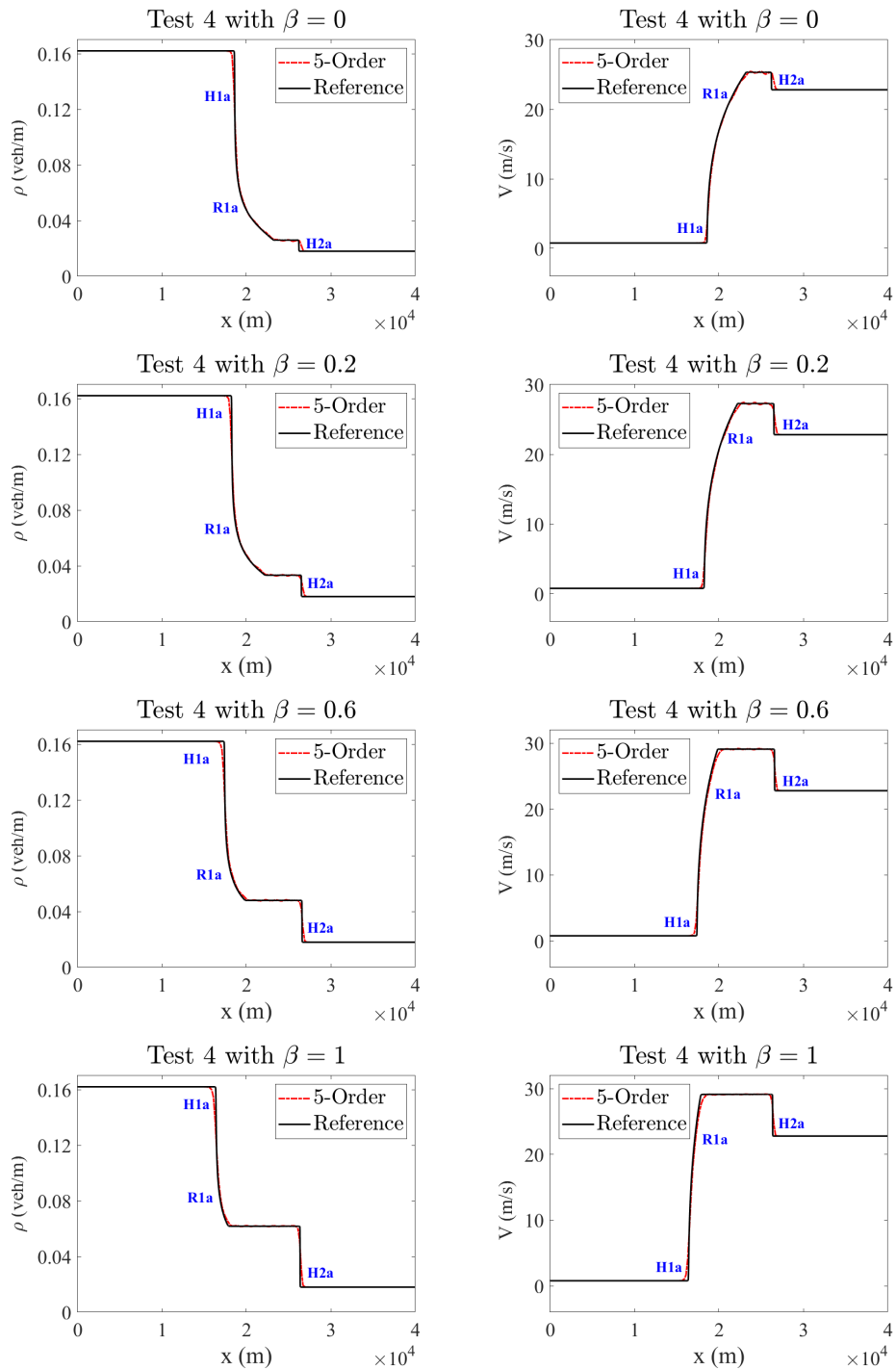Figure 12: The 2003 Zhang model, Case A, Test 3: Same as in Figs. 10 and 11.

Figure 13: The 2003 Zhang model, Case A, Test 4: Same as in Figs. 10-12.

In Tests 1 and 2, traffic condition is initially heavier in the downstream ($x > x_0$), and the 1-wave is a shock wave that travels backward as the upstream vehicles decelerate. In contrast, in both tests, the condition $|\eta(\rho_R)| << 1$ applies for the initial Riemann data (see Fig. 7), and the 2-wave is a shock that travels forward. In both Tests 1 and 2, only one intermediate state arises between the two shocks. We note that regardless of the choice of $\beta$, the 1-wave is always a deceleration shock, referred to as H1d. However, the 2-shocks are not of the same type. In Test 1, the value of $\beta$ affects the intermediate states and as well as the type of the 2-shocks. For instance, for $\beta = 0$ and 0.2, the traffic density at the intermediate state becomes greater than that of downstream, where the 2-wave is an acceleration shock (referred to as H2a shock) that causes the downstream vehicles to speed up. In contrast, for the larger $\beta$ values ($\beta = 0.6$ and $\beta = 1$), the intermediate state occurs at a density smaller than that of the downstream. This observation can be explained by the fact that with an increase in $\beta$, the magnitude of propagation speed $(\beta + \sqrt{1+\beta^2})|C(\rho)|$ in the moving coordinate increases, suggesting that drivers respond to traffic condition ahead more quickly. As a result, 1-shocks propagate backward faster, and the intermediate traffic becomes less congested and faster than the downstream one. In these cases, the 2-shocks are deceleration shocks (referred to as H2d), which force the downstream vehicles to slow down. Similar points apply to Test 2 regarding the impact of $\beta$ on the intermediate states. However, in Test 2, downstream traffic is highly congested while travels faster than the "equilibrium" speed. In this case, the intermediate state always occurs at a density smaller than that of the downstream. With an increase in $\beta$, the density in the intermediate state decreases and 1-shocks propagate backward faster. We note that in Test 2, 2-shocks are deceleration shocks (H2d) for all $\beta$; see Fig. 11.

We now discuss the numerical results for Tests 3 and 4 from a physical perspective. In both cases, traffic condition is highly congested in the upstream ($x < x_0$) as $|\eta(\rho_L)| \ll 1$, whereas on the right side, traffic density is very light. In both cases, the 1-wave is a composite acceleration wave as the upstream vehicles adapt their speed to that of downstream. This wave consists of a shock (referred to as H1a) in larger density ranges, joint with a rarefaction (referred to as R1a) in smaller density ranges. In Tests 3 and 4, intermediate states arise between the 1- and 2-waves. The results show that the parameter $\beta$ affects the 2-waves more significantly. To elaborate, we note that in Test 3, $\beta = 0$ results in a 2-rarefaction deceleration wave (referred to as R2d) that causes the downstream vehicles, which are traveling faster than the "equilibrium" speed, to slow down. However, as $\beta$ increases, the acceleration rate increases within the R1a waves, and thereby causing the intermediate states to be faster than the downstream states. Consequently, the 2-waves are acceleration shocks (referred to as H2a), which force the downstream vehicles to speed up. Similar points apply to the results for Test 4, but we note that regardless of $\beta$, the 2-waves are always acceleration shocks (H2a). This is because in the initial downstream traffic speed is slower then "equilibrium" one. Finally, one observes that in both Tests 3 and 4, with an increase in $\beta$, the magnitude of discontinuity increases for the H2a shocks.

**Case B.**   We now consider the system (5.10) and demonstrate the ability of the proposed 5-Order Scheme to handle the relaxation and nonlinear diffusion terms. In our numerical example, we set the relaxation time as $\tau = 40s$ from a typical range. We compute the numerical solutions on the computational domain $[0,40000]$ using 200 uniform cells until the final time $t = 200s$. The numerical results of the 5-Order scheme for Tests 2 and 3 from Table 5 are shown in Fig. 14 together with the reference solution computed by the 5-Order Scheme on a finer mesh with 4000 uniform cells. As one can see, the proposed 5-Order scheme can achieve high resolution even when a coarse mesh is used. The obtained results are non-oscillatory since both the diffusion and relaxation terms can have smoothing effects and suppress the inherent numerical oscillations. Therefore, there is no need to add the AAV in such cases.

# 6   Conclusions

Non-equilibrium continuum traffic flow models describe the spatio-temporal evolution of traffic states with the help of hyperbolic systems, in which separate PDEs are employed for flow-continuity and speed adaptation equations. While many existing non-equilibrium models can be presented in the conservative form, behavioral non-equilibrium ones derived from car-following models are often non-conservative. Meanwhile, conventional approaches for analytical and numerical investigations of continuum traffic flow models heavily rely on the presence of conservative form. As a result, lack of conservation property has remained an obstacle for both numerical solution and further development of behavioral non-equilibrium models.

In order to overcome this obstacle, we have developed a new fifth-order finite-difference alternative weighted essentially non-oscillatory (A-WENO) scheme based on the path-conservative central-upwind (PCCU) method to solve non-equilibrium traffic models based on their non-conservative form. We have first applied the second-order finite-volume (FV) PCCU scheme to the traffic flow models, and then extended it to the fifth order of accuracy using the finite-difference A-WENO framework. We have demonstrated the scheme's performance for three non-equilibrium traffic models, including the Aw-Rascle-Zhang model, the 1998 Zhang behavioral model, and the 2003 Zhang non-conservative behavioral model. We have verified the proposed scheme's robustness regarding capturing the overall solution, sharpness and accuracy, and capability of suppressing the inherent numerical oscillations. The scheme has also been compared with the corresponding second-order FV PCCU scheme. In order to prevent appearance of large magnitude oscillations, the adaptive artificial viscosity (AAV) has been added to the proposed A-WENO PCCU scheme in some of the numerical examples. The AAV is made to be proportional to the weak local residual.

The proposed A-WENO PCCU scheme paves the way for developing new and better behavioral non-equilibrium traffic models. In contrast to many purely physical systems, traffic flow involves human drivers, and numerous empirical studies have estab-

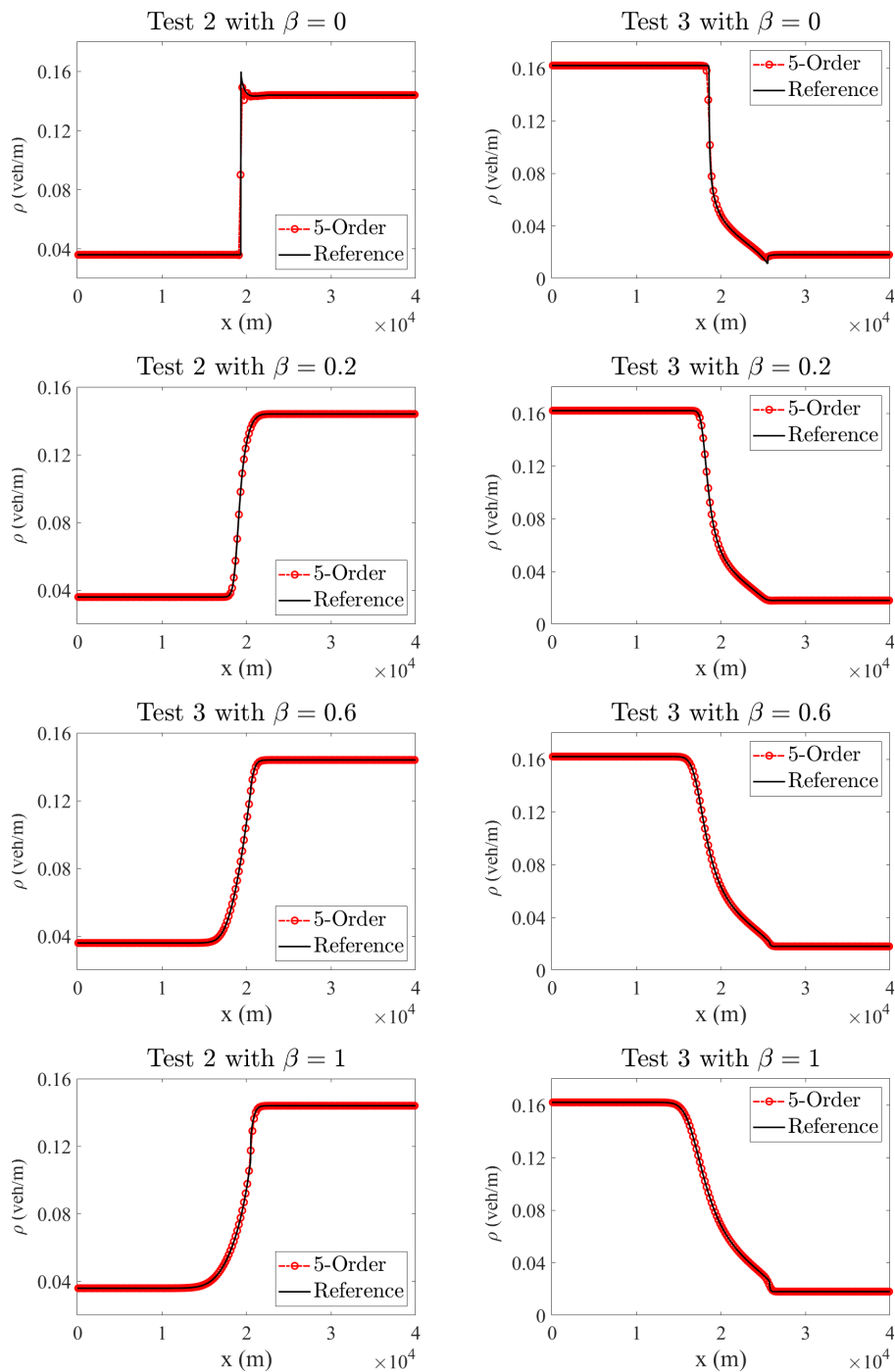Figure 14: The 2003 Zhang model, Case B: Density ($\rho$) and velocity ($V$) profiles at $t = 200s$ computed by the 5-Order Scheme. The computations have been conducted for $\beta = 0$ (first row), 0.2 (second row), 0.6 (third row) and 1 (fourth row).

lished profound linkages between such human factors and complex traffic phenomena, underscoring the need to develop new and better behavioral models that can adequately capture the impacts of complex human factors on traffic flow dynamics. Recently, a unifiable framework has been developed in [30] to derive non-equilibrium continuum models from car-following models, which can be used as a guideline to develop behavioral continuum models with respect to human psychological factors. However, such a practice is likely to result in the loss of the conservative form with the associated inherent numerical difficulties that perhaps have hindered the development of such behavioral models until very recently. In this paper, we have shown that such difficulties can be overcome by the proposed A-WENO PCCU scheme.

There is a couple of future directions to this work. First, there is a need to couple the proposed A-WENO PCCU scheme with more robust schemes for source terms near on-ramp areas. Meanwhile, we are currently implementing the proposed A-WENO PCCU scheme to solve the Riemann problem for the novel behavioral continuum model (non-equilibrium traffic model based on risk allostasis theory, that is, NET-RAT), recently developed in [46].

## Acknowledgments

## A   Fifth-order WENO-Z interpolant

In this appendix, we briefly describe the fifth-order WENO-Z interpolant from [12,28,41, 63]. Assume that the point values $W_j$ of a certain quantity $W$ at the grid points $x = x_j$ are available. We now show how to obtain an interpolated value of $W$ at $x = x_{j+\frac{1}{2}}-$, denoted by $W_{j+\frac{1}{2}}^-$. The right-sided value $W_{j+\frac{1}{2}}^+$ can then be obtained in the mirror-symmetric way.

The value $W_{j+\frac{1}{2}}^-$ is computed using a weighted average of the three parabolic interpolants $\mathcal{P}_0(x)$, $\mathcal{P}_1(x)$ and $\mathcal{P}_2(x)$ obtained using the stencils $[x_{j-2}, x_{j-1}, x_j]$, $[x_{j-1}, x_j, x_{j+1}]$ and $[x_j, x_{j+1}, x_{j+2}]$, respectively:

$$W_{j+\frac{1}{2}}^- = \sum_{k=0}^{2} \omega_k \mathcal{P}_k(x_{j+\frac{1}{2}}), \tag{A.1}$$

where

$$\mathcal{P}_0(x_{j+\frac{1}{2}}) = \frac{3}{8} W_{j-2} - \frac{5}{4} W_{j-1} + \frac{15}{8} W_j,$$

$$\mathcal{P}_1(x_{j+\frac{1}{2}}) = -\frac{1}{8}W_{j-1} + \frac{3}{4}W_j + \frac{3}{8}W_{j+1},$$

$$\mathcal{P}_2(x_{j+\frac{1}{2}}) = \frac{3}{8}W_j + \frac{3}{4}W_{j+1} - \frac{1}{8}W_{j+2}.$$

The weights $\omega_k$ are computed by

$$\omega_k = \frac{\alpha_k}{\alpha_0 + \alpha_1 + \alpha_2}, \quad \alpha_k = d_k\left[1 + \left(\frac{\tau_5}{\beta_k + \varepsilon}\right)^p\right], \quad \tau_5 = |\beta_2 - \beta_0|, \tag{A.2}$$

with $d_0 = \frac{1}{16}, d_1 = \frac{5}{8}, d_2 = \frac{5}{16}$, and the smoothness indicators $\beta_k$ in (A.2) for the corresponding parabolic interpolants $\mathcal{P}_k(x)$ are defined by

$$\beta_k = \sum_{\ell=1}^{2}(\Delta x)^{2\ell-1}\int_{x_{j-\frac{1}{2}}}^{x_{j+\frac{1}{2}}}\left(\frac{\partial^\ell \mathcal{P}_k}{\partial x^\ell}\right)^2 \mathrm{d}x, \quad k=0,1,2. \tag{A.3}$$

Evaluating the integrals in (A.3), we obtain

$$\beta_0 = \frac{13}{12}\left(W_{j-2} - 2W_{j-1} + W_j\right)^2 + \frac{1}{4}\left(W_{j-2} - 4W_{j-1} + 3W_j\right)^2,$$

$$\beta_1 = \frac{13}{12}\left(W_{j-1} - 2W_j + W_{j+1}\right)^2 + \frac{1}{4}\left(W_{j-1} - W_{j+1}\right)^2, \tag{A.4}$$

$$\beta_2 = \frac{13}{12}\left(W_j - 2W_{j+1} + W_{j+2}\right)^2 + \frac{1}{4}\left(3W_j - 4W_{j+1} + W_{j+2}\right)^2.$$

Finally, in all of the numerical examples reported in Section 5, we have used $p=2$ and $\varepsilon = 10^{-12}$.

## References

[1] A. Aw, Existence of a global entropic weak solution for the Aw-Rascle model, Int. J. Evol. Equ., 9 (2014), 53–70.

[2] A. Aw, A. Klar, T. Materne and M. Rascle, Derivation of continuum traffic flow models from microscopic follow-the-leader models, SIAM J. Appl. Math., 63 (2002), 259–278.

[3] A. Aw and M. Rascle, Resurrection of "second order" models of traffic flow, SIAM J. Appl. Math., 60 (2000), 916–938.

[4] S. Benzoni-Gavage and R. M. Colombo, An $n$-populations model for traffic flow, European J. Appl. Math., 14 (2003), 587–612.

[5] S. Blandin and P. Goatin, Well-posedness of a conservation law with non-local flux arising in traffic flow modeling, Numer. Math., 132 (2016), 217–241.

[6] M. J. Castro, T. Morales de Luna and C. Parés, Well-balanced schemes and path-conservative numerical methods, in Handbook of numerical methods for hyperbolic problems, vol. 18 of Handb. Numer. Anal., Elsevier, North-Holland, Amsterdam, 2017, 131–175.

[7] M. Castro, A. Kurganov and T. Morales de Luna, Path-conservative central-upwind schemes for nonconservative hyperbolic systems, ESAIM Math. Model. Numer. Anal., 53 (2019), 959–985.

[8] D. Chen, J. A. Laval, S. Ahn and Z. Zheng, Microscopic traffic hysteresis in traffic oscillations: A behavioral perspective, Transport. Res. B-Meth., 46 (2012), 1440–1453.

[9] Y. Chen, A. Kurganov, M. Lei and Y. Liu, An adaptive artificial viscosity method for the Saint-Venant system, in Recent developments in the numerics of nonlinear hyperbolic conservation laws, vol. 120 of Numer. Fluid Mech. Multidiscip. Des., Springer, Heidelberg, 2013, 125–141.

[10] F. A. Chiarello, J. Friedrich, P. Goatin, S. Göttlich and O. Kolb, A non-local traffic flow model for 1-to-1 junctions, European J. Appl. Math., 31 (2020), 1029–1049.

[11] F. A. Chiarello and P. Goatin, Non-local multi-class traffic flow models, Netw. Heterog. Media, 14 (2019), 371–387.

[12] S. Chu, A. Kurganov and M. Na, Fifth-order A-WENO schemes based on the path-conservative central-upwind method, J. Comput. Phys., 469 (2022), Paper No. 111508, 22 pp.

[13] R. M. Colombo, A $2 \times 2$ hyperbolic traffic flow model, Math. Comput. Modelling, 35 (2002), 683–688.

[14] C. F. Daganzo, Requiem for second-order fluid approximations of traffic flow, Transport. Res. B-Meth., 29 (1995), 277–286.

[15] C. F. Daganzo, A continuum theory of traffic dynamics for freeways with special lanes, Transport. Res. B-Meth., 31 (1997), 83–102.

[16] C. F. Daganzo, A behavioral theory of multi-lane traffic flow. Part I: Long homogeneous freeway sections, Transport. Res. B-Meth., 36 (2002), 131–158.

[17] G. Dal Maso, P. G. Lefloch and F. Murat, Definition and weak stability of nonconservative products, J. Math. Pures Appl., 74 (1995), 483–548.

[18] J. M. del Castillo, Three new models for the flow–density relationship: Derivation and testing for freeway and urban data, Transportmetrica, 8 (2012), 443–465.

[19] W. S. Don, D.-M. Li, Z. Gao and B.-S. Wang, A characteristic-wise alternative WENO-Z finite difference scheme for solving the compressible multicomponent non-reactive flows in the overestimated quasi-conservative form, J. Sci. Comput., 82 (2020), Paper No. 27, 24 pp.

[20] J. Friedrich, O. Kolb and S. Göttlich, A Godunov type scheme for a class of LWR traffic flow models with non-local flux, Netw. Heterog. Media, 13 (2018), 531–547.

[21] S. Gottlieb, D. Ketcheson and C.-W. Shu, Strong Stability Preserving Runge-Kutta and Multistep Time Discretizations, World Scientific Publishing Co. Pte. Ltd., Hackensack, NJ, 2011.

[22] S. Gottlieb, C.-W. Shu and E. Tadmor, Strong stability-preserving high-order time discretization methods, SIAM Rev., 43 (2001), 89–112.

[23] A. K. Gupta and V. Katiyar, A new anisotropic continuum model for traffic flow, Physica A., 368 (2006), 551–559.

[24] A. K. Gupta and V. Katiyar, A new multi-class continuum model for traffic flow, Transportmetrica, 3 (2007), 73–85.

[25] E. N. Holland and A. W. Woods, A continuum model for the dispersion of traffic on two-lane roads, Transport. Res. B-Meth., 31 (1997), 473–485.

[26] S. P. Hoogendoorn and P. H. Bovy, Continuum modeling of multiclass traffic flow, Transport. Res. B-Meth., 34 (2000), 123–146.

[27] R. Jiang, Q.-S. Wu and Z.-J. Zhu, A new continuum model for traffic flow and numerical tests, Transport. Res. B-Meth., 36 (2002), 405–419.

[28] Y. Jiang, C.-W. Shu and M. Zhang, An alternative formulation of finite difference weighted ENO schemes with Lax-Wendroff time discretization for conservation laws, SIAM J. Sci. Comput., 35 (2013), A1137–A1160.

[29] W.-L. Jin, A kinematic wave theory of lane-changing traffic flow, Transport. Res. B-Meth., 44 (2010), 1001–1021.

[30] W.-L. Jin, On the equivalence between continuum and car-following models of traffic flow, Transport. Res. B-Meth. 93 (2016), 543–559.

[31] S. Karni, A. Kurganov, Local error analysis for approximate solutions of hyperbolic conservation laws, Adv. Comput. Math., 22 (2005), 79–99.

[32] S. Karni, A. Kurganov and G. Petrova, A smoothness indicator for adaptive algorithms for hyperbolic systems, J. Comput. Phys., 178 (2002), 323–341.

[33] A. Kurganov and C.-T. Lin, On the reduction of numerical dissipation in central-upwind schemes, Commun. Comput. Phys., 2 (2007), 141–163.

[34] A. Kurganov and Y. Liu, New adaptive artificial viscosity method for hyperbolic systems of conservation laws, J. Comput. Phys., 231 (2012), 8114–8132.

[35] J. P. Lebacque, The Godunov scheme and what it means for first order traffic flow models, Transportation and Traffic Theory, Proc., 13th ISTTT, J. B. Lesort, ed., Pergamon, Oxford, England, 1996.

[36] J.-P. Lebacque, S. Mammar and H. Haj-Salem, The Aw-Rascle and Zhang's model: Vacuum problems, existence and regularity of the solutions of the Riemann problem, Transport. Res. B-Meth., 41 (2007), 710–721.

[37] J.-P. Lebacque, S. Mammar and H. Haj-Salem, Generic second order traffic flow modelling, Transportation and Traffic Theory, 207(2007), 755–776.

[38] P. G. Lefloch, Graph solutions of nonlinear hyperbolic systems, J. Hyperbolic Differ. Equ., 1 (2004), 643–689.

[39] P. G. LeFloch, Hyperbolic systems of conservation laws, Lectures in Mathematics ETH Zürich, Birkhäuser Verlag, Basel, 2002.

[40] M. J. Lighthill and G. B. Whitham, On kinematic waves. II. A theory of traffic flow on long crowded roads, Proc. Roy. Soc. London Ser. A, 229 (1955), 317–345.

[41] H. Liu, A numerical study of the performance of alternative weighted ENO methods based on various numerical fluxes for conservation law, Appl. Math. Comput., 296 (2017), 182–197.

[42] S. Mammar, J.-P. Lebacque and H. Haj-Salem, Riemann problem resolution and Godunov scheme for the Aw-Rascle-Zhang model, Transport. Sci., 43 (2009), 531–545.

[43] S. Mohammadian, Freeway traffic flow dynamics and safety: A behavioural continuum framework, PhD thesis, Queensland University of Technology, 2021.

[44] S. Mohammadian, A. M. Moghaddam and A. Sahaf, On the performance of HLL, HLLC, and Rusanov solvers for hyperbolic traffic models, Comput. & Fluids, 231 (2021), No. 105161, 20 pp.

[45] S. Mohammadian and F. van Wageningen-Kessels, Improved numerical method for Aw-Rascle type continuum traffic flow models, Transp. Res. Rec., 2672 (2018), 262–276.

[46] S. Mohammadian, Z. Zheng, M. M. Haque and A. Bhaskar, NET-RAT: Non-equilibrium traffic model based on risk allostasis theory, submitted.

[47] S. Mohammadian, Z. Zheng, M. M. Haque and A. Bhaskar, Continuum modelling of freeway traffic flows in the era of connected and automated vehicles: A critical perspective and research needs, arXiv preprint arXiv:2111.04955.

[48] S. Mohammadian, Z. Zheng, M. M. Haque and A. Bhaskar, Performance of continuum models for realworld traffic flows: Comprehensive benchmarking, Transport. Res. B-Meth., 147 (2021), 132–167.

[49] D. Ngoduy and R. Liu, Multiclass first-order simulation model to explain non-linear traffic phenomena, Physica A, 385 (2007), 667–682.

[50] T. Nonomura and K. Fujii, Characteristic finite-difference WENO scheme for multicompo-
nent compressible fluid analysis: overestimated quasi-conservative formulation maintain-
ing equilibriums of velocity, pressure, and temperature, J. Comput. Phys., 340 (2017), 358–
388.

[51] M. Papageorgiou, Some remarks on macroscopic traffic flow modelling, Transport. Res. A-
Pol., 32 (1998), 323–329.

[52] C. Parés, Path-conservative numerical methods for nonconservative hyperbolic systems in
numerical methods for balance laws, vol. 24 of Quad. Math., Dept. Math., Seconda Univ.
Napoli, Caserta, 2009, 67–121.

[53] Z. Qian, J. Li, X. Li, H. M. Zhang and H. Wang, Modeling heterogeneous traffic flow: A
pragmatic approach, Transport. Res. B-Meth., 99 (2017), 183–204.

[54] P. I. Richards, Shock waves on the highway, Operations Res., 4 (1956), 42–51.

[55] S. Mohammad and Z. Zheng, Incorporating human-factors in car-following models: A re-
view of recent developments and research needs, Transport. Res. C-Emer., 48 (2014), 379–
403.

[56] S. Mohammad, Z. Zheng, M. M. Haque and S. Washington, Understanding the mechanism
of traffic hysteresis and traffic oscillations through the change in task difficulty level, Trans-
port. Res. B-Meth., 105 (2017), 523–538.

[57] A. Sopasakis and M. A. Katsoulakis, Stochastic modeling and simulation of traffic flow:
Asymmetric single exclusion process with Arrhenius look-ahead dynamics, SIAM J. Appl.
Math., 66 (2006), 921–944.

[58] P. K. Sweby, High resolution schemes using flux limiters for hyperbolic conservation laws,
SIAM J. Numer. Anal., 21 (1984), 995–1011.

[59] M. Treiber, A. Hennecke and D. Helbing, Derivation, properties, and simulation of a gas-
kinetic-based, nonlocal traffic model, Phys. Rev. E., 59 (1999), 239–253.

[60] T. Martin, K. Arne and H. Dirk, Three-phase traffic theory and two-phase models with a
fundamental diagram in the light of empirical stylized facts, Transport. Res. B-Meth., 44
(2010), 983–1000.

[61] J. W. C. van Lint, S. P. Hoogendoorn and M. Schreuder, Fastlane: New multiclass first-order
traffic flow model, Transport. Res. Rec., 2088 (2008), 177–187.

[62] F. van Wageningen-Kessels, H. van Lint, S. P. Hoogendoorn and K. Vuik, New generic multi-
class kinematic wave traffic flow model: Model development and analysis of its properties,
Transport. Res. Rec., 2422 (2014), 50–60.

[63] B.-S. Wang, P. Li, Z. Gao and W. S. Don, An improved fifth order alternative WENO-Z finite
difference scheme for hyperbolic conservation laws, J. Comput. Phys., 374 (2018), 469–477.

[64] K. Yuan and H. K. Lo, Multiclass traffic flow dynamics: An endogenous model, Transport.
Sci., 55 (2021), 456–474.

[65] H. M. Zhang, A theory of nonequilibrium traffic flow, Transport. Res. B-Meth., 32 (1998),
485–498.

[66] H. M. Zhang, Analyses of the stability and wave properties of a new continuum traffic the-
ory, Transport. Res. B-Meth., 33 (1999), 399–415.

[67] H. M. Zhang, A mathematical theory of traffic hysteresis, Transport. Res. B-Meth., 33 (1999),
1–23.

[68] H. M. Zhang, Structural properties of solutions arising from a nonequilibrium traffic flow
theory, Transport. Res. B-Meth., 34 (2000), 583–603.

[69] H. M. Zhang, A finite difference approximation of a non-equilibrium traffic flow model,
Transport. Res. B-Meth., 35 (2001), 337–365.

[70] H. M. Zhang, A non-equilibrium traffic model devoid of gas-like behavior, Transport. Res. B-Meth., 36 (2002), 275–290.

[71] H. M. Zhang, Driver memory, traffic viscosity and a viscous vehicular traffic flow model, Transport. Res. B-Meth., 37 (2003), 27–41.

[72] H. M. Zhang, Comment on "On the controversy around Daganzo's requiem for and Aw-Rascle's resurrection of second-order traffic flow models" by D. Helbing and A. F. Johansson, Eur. Phys. J. B, 69 (2009), 563–568.